Atmospheric Research 311 (2024) 107724

Contents lists available at ScienceDirect

Atmospheric Research

journal homepage: www.elsevier.com/locate/atmosres

An extreme precipitation event over Dronning Maud Land, East Antarctica - A case study of an atmospheric river event using the Polar WRF Model

Sibin Simon [a,b,*], John Turner [c], Thamban Meloth [a], Pranab Deb [d], Irina V. Gorodetskaya [e], Matthew Lazzara [f,g]

[a] National Centre for Polar and Ocean Research, Goa, India
[b] School of Earth Ocean and Atmospheric Sciences, Goa University, Goa, India
[c] Retired, Cambridge, UK
[d] Centre for Ocean, River, Atmosphere and Land Sciences, Indian Institute of Technology Kharagpur, Kharagpur, West Bengal, India
[e] CIIMAR - Interdisciplinary Centre of Marine and Environmental Research of the University of Porto, Matosinhos, Portugal
[f] Antarctic Meteorological Research and Data Center, Space Science and Engineering Center, University of Wisconsin–Madison, Madison, WI, USA
[g] Department of Physical Sciences, School of Engineering, Science, and Mathematics, Madison Area Technical College, Madison, WI, USA

ARTICLE INFO

Keywords:
Extreme precipitation event
Atmospheric rivers
East Antarctica
High-pressure ridge
Jet streak
Polar WRF

ABSTRACT

Extreme precipitation events (EPEs) are crucial in Antarctica, impacting the Antarctic ice sheet's surface mass balance and stability. Comprehensive case studies are essential for better understanding these events and the underlying processes driving them. Here, we investigate an extreme snowfall event in Dronning Maud Land (DML), East Antarctica on November 8 and 9, 2015. This event contributed approximately 22 % of the annual accumulation in less than two days and exhibited high spatial variability in precipitation distribution. We employed a high-resolution atmospheric model specifically optimized for the polar regions (Polar WRF) and ERA5 reanalysis data to analyze the event in detail. Our findings highlight the importance of a blocking high-pressure ridge of record strength that effectively blocked and diverted a strong extratropical cyclone into DML, ultimately leading to the heavy snowfall event. The sudden deepening of the cyclone was initiated by a 'jet streak' in the upper atmosphere that steered the system southeastwards towards the Antarctic coast. Notably, we observed an anomalously high poleward moisture transport in the form of a strong atmospheric river on November 7, 2015. This atmospheric river originated in the South Atlantic Ocean and tracked poleward from the 30°S-40°S latitude band. Vertical cross-sections of the model outputs indicate that most of the precipitation was concentrated in regions with steep orography along the path of the atmospheric river. This interaction between the atmospheric river and the steep terrain led to the uplift of maritime air, resulting in heavy snowfall. This study highlights the significance of extreme upper and lower atmospheric conditions in driving intense moisture transport towards coastal DML. The interaction between the atmospheric river and the steep orography contributed to heavy snowfall, underscoring the importance of considering orographic influences in understanding EPEs in Antarctica.

1. Introduction

Understanding precipitation characteristics in Antarctica is crucial for studying the dynamics and ice sheet growth, which is critical in mitigating rising sea levels (Lenaerts et al., 2013; Medley and Thomas, 2019). Recent studies emphasize that extreme snowfall variability controls coastal Antarctica's short-term sea level contribution (Davison et al., 2023). The nature and duration of precipitation differ significantly between the interior of the continent and the coastal region. Accumulation over coastal Antarctica is controlled by episodic, short-lived, high-precipitation events (Bromwich, 1988; Gorodetskaya et al., 2014, 2015; Schlosser et al., 2010), and studies show that these short-lived synoptic events can explain the recent and expected positive trends in Antarctic precipitation (Dalaiden et al., 2020). Extreme precipitation events (EPEs) contribute a large portion (>40 %) of annual snowfall in just a few days across much of the continent (Noone et al., 1999; Turner et al., 2019). These EPEs are one of the major controlling factors of sudden changes in surface mass balance and surface height

* Corresponding author at: National Centre for Polar and Ocean Research, Goa, India.
E-mail address: sibin@ncpor.res.in (S. Simon).

https://doi.org/10.1016/j.atmosres.2024.107724
Received 16 January 2024; Received in revised form 17 August 2024; Accepted 9 October 2024
Available online 10 October 2024

over most of the West (Adusumilli et al., 2021) and East (Boening et al., 2012; Gorodetskaya et al., 2014; Lenaerts et al., 2013) Antarctic coastal regions. Large temperature variations are also associated with these events, causing surface melt (Gorodetskaya et al., 2023; Wille et al., 2019; Zou et al., 2022), decreasing the stability of the ice shelves (Wille et al., 2022) and record-setting temperature values (Bozkurt et al., 2018; Gorodetskaya et al., 2023; Wille et al., 2023).

These high precipitation events are often associated with intense atmospheric rivers (ARs), which are long, narrow bands of high moisture transport that originate in tropical and subtropical latitudes (Gorodetskaya et al., 2014; Maclennan and Lenaerts, 2021; Swetha Chittella et al., 2022; Terpstra et al., 2021). These ARs lead to 10–20 % of the total annual Antarctic precipitation and are associated with 35–45 % of EPEs when considering the 95th percentile criteria (Wille et al., 2021). Dronning Maud Land (DML) is influenced by many ARs that explain 77 % of the precipitation variability (Baiman et al., 2023). Wille et al. (2021) identified an increasing trend in ARs over DML from 1980 to 2018, with anomalous changes observed in 2009 and 2011 (Gorodetskaya et al., 2014). Using a case study of an intense AR in East Antarctica during February 2011, Terpstra et al. (2021) found that the sub-tropics were a primary moisture source for Antarctic precipitation. The extreme state of lower-tropospheric variables in the vertical profile emphasizing extreme moisture transport and temperatures during AR events was demonstrated by Gorodetskaya et al. (2020) using radiosonde measurements over DML. During AR events the dipole structure of low-pressure cyclones to the west and high-pressure anticyclones to the east is evident, which is similar in most of the EPEs over East Antarctica (Terpstra et al., 2021; Welker et al., 2014; Yu et al., 2018).

The large-scale circulation of the Southern Hemisphere has undergone notable changes in recent decades. Reanalysis data have revealed significant increases in the occurrence of deep mid-latitude cyclones and a poleward shift in their tracks (Grise et al., 2019; Solman and Orlanski, 2014; Wang et al., 2016). Particularly during the Austral summer, there is a noticeable increasing trend in number of cyclones south of 60°S, as observed in different reanalysis data (Grieger et al., 2018). Additionally, there is a pronounced positive trend in the number of cyclones, especially in the high latitudes of the South Atlantic Ocean (Reboita et al., 2015). In conjunction with this, during Austral summer, the South Atlantic Ocean has experienced increased high-pressure blocking activity (Dennison et al., 2016). This alters the path of mid-latitude

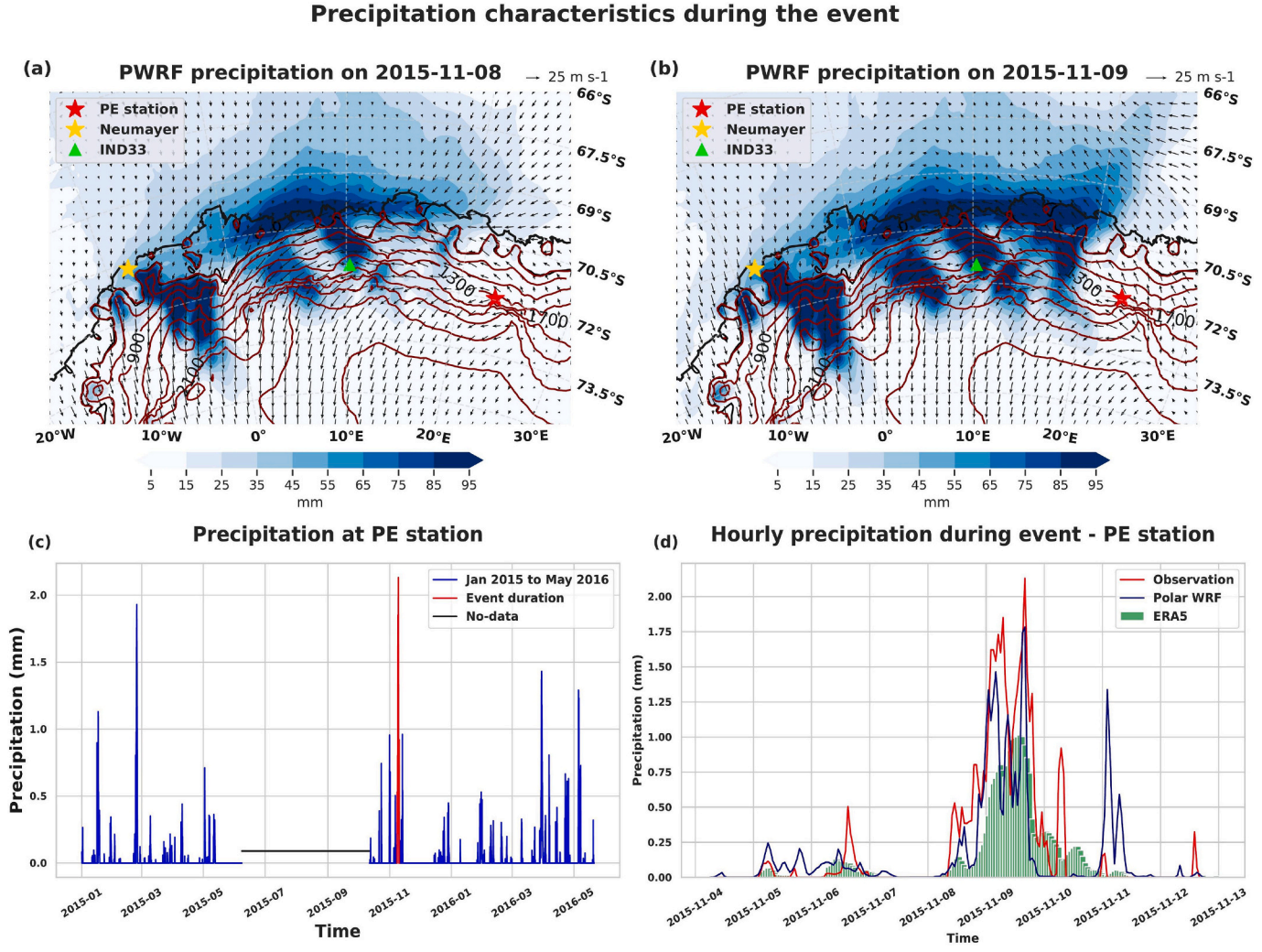

Fig. 1. (a) Spatial distribution of daily accumulated precipitation (shading, unit (mm)) from Polar WRF model domain with 9 km resolution for 8th November 2015. The orography (red lines, units (m)) of the DML region and wind vectors are overlaid. Also, the ice core location (IND33) and locations of Neumayer and Princess Elisabeth station (PE) stations are marked. (b) same as (a) but for 9th November 2015. (c) Hourly precipitation reported at the PE station derived from MRR measurements from January 2015 to May 2016 (blue lines, units (mm/h)). A red line marks the precipitation for the event duration, and the data gap area is marked with a black horizontal line. (d) Hourly precipitation (green bar, units (mm)) derived from ERA5 for the event days and hourly precipitation observed at the PE station (red line, units (mm)) and simulated using the Polar WRF model (blue line, units (mm)). DML: Dronning Maud Land, MRR: Metek's Micro Rain Radar. (For interpretation of the references to colour in this figure legend, the reader is referred to the web version of this article.)

cyclones, directing them towards the coast of East Antarctica.

These EPEs impact Antarctic atmospheric conditions, glaciological conditions, and ice core data records (Noone et al., 1999; Schlosser et al., 2017). Factors such as moisture from northern latitudes, high temperatures during the events, and post-deposition processes due to strong winds can introduce bias in ice core climate records, particularly concerning EPE frequency and magnitude (Schlosser et al., 2010; Servettaz et al., 2020; Turner et al., 2019). The region's orography also influences significantly the snowfall distribution and wind-driven redistribution (Dattler et al., 2019; Lenaerts et al., 2012; Souverijns et al., 2018). The influence of orography also implies that very little precipitation can be possible even during a strong AR event due to snowfall sublimation in the lower troposphere in response to the generation of orographic gravity waves (Gehring et al., 2022) and due to katabatic winds (Grazioli et al., 2017).

This study analyses a heavy precipitation event at the beginning of Austral summer on November 8 and 9, 2015. This event was one of the most significant precipitation events at the ice core site (IND33–71.51°S,10.15°E, Fig. 1) (Ejaz et al., 2021) in coastal DML (20°W to 45°E). Significantly, this event was associated with an intense AR, within the top 1 % of ARs, identified through the atmospheric river tracking technique developed by Wille et al. (2021). Our primary goals are to determine the extreme conditions during this event, follow the evolution of the synoptic-scale environment, and elucidate the pathways of intense moisture transport. This investigation employs a combination of ground-based in-situ and remote sensing observations, reanalysis data, and satellite imagery. Additionally, using a high-resolution regional atmospheric model (Polar WRF), we explore the role of coastal orography on the distribution of precipitation during this event.

2. Data and methods

2.1. Reanalysis data

We used the European Centre for Medium-range Weather Forecasts (ECMWF) ERA-5 reanalysis (Hersbach et al., 2020) for this climatological and synoptic analysis in this study. The data are taken at a spatial resolution of 0.25° x 0.25° and hourly temporal resolution. The variables, including precipitation, mean sea level pressure (MSLP), zonal (U), and meridional (V) wind components at 10-m height, and air temperature at 2 m, are taken at single levels. Vertically integrated water vapor transport (IVT) was calculated using available vertically integrated zonal and meridional components of moisture flux values. Geopotential height, U and V components of winds, and specific humidity are taken at different pressure levels. We have extracted precipitation data from three additional reanalysis products with different spatial and temporal resolutions to compare their representation of precipitation distribution during the EPE. The reanalysis used were MERRA2 (0.5° x 0.625°, hourly), JRA55 (1.25° x 1.25°, 6-hourly), CFSv2 (0.5° x 0.5°, hourly) for EPE day November 8, 2015.

AR detection: The AR detection technique uses locations of vIVT (the meridional component of integrated vapor transport) between 37.5°S and 80°S, surpassing the 98th percentile of all monthly vIVT values per grid cell from 1980 to 2021. A long, narrow band of vIVT values over this threshold that stretches at least 20° in the meridional direction was considered to be an AR by the algorithm. For more information, see Wille et al. (2021).

Extreme values detection: EPE days are also defined as the precipitation days (precipitation >0.02 mm) exceeding precipitation values greater than the 95th percentile value. To assess the extreme nature of this event, we identified the regions that exhibited extreme values before and during the heavy precipitating days. The extreme values were considered as those exceeding the 95th and 99th percentiles and less than the 5th and 1st percentiles compared with daily data for 1979–2018 for each latitude-longitude grid. The variables geopotential height at 500mb, MSLP, wind component, IVT, precipitation, and 2 m temperature were analyzed to determine the extreme conditions during this event (section 3.2).

2.2. Satellite composite imagery

The Antarctic satellite composite imagery is a mosaic of geostationary and polar orbiting satellite imagery (Kohrs et al., 2014; Lazzara et al., 2003). Data from the geostationary satellites such as GOES (Geostationary Operational Environmental Satellite), Himawari, and Meteosat are combined with polar-orbiting satellites such as the NOAA (National Oceanic and Atmospheric Administration, also known as POES or Polar-orbiting Environmental Satellite), Terra/Aqua, and Metop satellites. They are combined utilizing a scheme to include the lowest parallax and highest resolution observational data into the product while keeping satellite calibration information. The composite is made hourly and is made over several spectral channels. This study uses infrared (IR - 10.7 μm) and water vapor composites (6.7 μm) to track the development of cloud and moisture characteristics.

2.3. Ground-based observations

The cloud/precipitation/meteorological observatory at the Belgian Princess Elisabeth (PE) research station, Dronning Maud Land, East Antarctica (Gorodetskaya et al., 2015), provided the precipitation readings during the studied EPE. The PE observatory is situated 180 km inland at 71°57′S and 23°21′E and has an elevation of 1392 m above mean sea level. The Metek's Micro Rain Radar, MRR-2, deployed at PE station (Fig. 1a) in February 2010, was used to calculate the precipitation rates. The precipitation reaching the surface was calculated by converting the associated effective reflectivity (Ze) to snowfall rates (SR) using various Ze-SR relationships for dry snow. Souverijns et al. (2017) provide detailed information on the calculation of Ze, SR, and the parameters of the Ze-SR relation used to process precipitation rate (mm/h).

The in-situ observations from automatic weather stations from the two coastal DML stations (Neumayer (Germany) at 70.645°S, 8.264°W, and PE (Belgium)) were also used for the comparison of Polar WRF model outputs. Neumayer station data were obtained as part of the Scientific Committee on Antarctic Research (SCAR) Reference Antarctic Data for Environmental Research (READER) project and subject to a strict quality control procedure (Turner et al., 2004). The available surface meteorological variables like precipitation, 2 m temperature, surface pressure, mean sea level pressure, wind speed, and direction were used for the model validation. Time series from the nearest grid points were subsampled to coincide with the temporal resolution of each station's observations. The correlation coefficient, bias, and root-mean-square error (RMSE) between model outputs at different domains and in-situ station observations were used to calculate a statistical measure of model performance.

2.4. Polar WRF model simulation

This study utilized data from the high-resolution regional atmospheric model, WRF version 4.1.1, optimized for the polar regions. The model incorporates improvements in representing essential variables such as sea ice fraction and thickness, snow depth, snow albedo, cloud radiative processes, and the heat transfer of ice and snow (Bromwich et al., 2013; Hines and Bromwich, 2008). The model used a 9 km parent domain within which an inner domain of 3 km resolution was nested in a polar-stereographic projection (Fig. S1). To provide the necessary surface, lateral boundary conditions, sea ice concentration, sea surface temperature, and other initial conditions, we utilized the ERA5 reanalysis. Additionally, geographic information was obtained from the WRF standard orography using the Global Multi-resolution Terrain Elevation Data 2010 (GMTED2010) (Danielson and Gesch, 2011), while land use and land cover data was from the Moderate Resolution Imaging Spectroradiometer (MODIS) dataset at a resolution of 1 km. This study

selected the parameterization schemes based on a sensitivity analysis that identifies the best-performing schemes in the planetary boundary layer (PBL), longwave radiation, and cloud microphysics for DML. The remaining physics schemes and configurations used in the study follow those employed in the Antarctic Mesoscale Forecast System (AMPS), a numerical weather prediction tool operated by the National Center for Atmospheric Research (NCAR) in the United States. Table 1 presents the physics options utilized in this study.

The 10-day long model simulation was conducted to study the EPE, and the simulation started from November 3, at 00:00 UTC, to November 12, 2015, at 18:00 UTC, with a temporal resolution of 1 h. The initial 24 h of data were considered a spin-up period and were not included in the subsequent analysis (Bromwich et al., 2013). Observed surface meteorological variables from coastal stations in DML, such as Neumayer and PE, were utilized to validate the model output. The model simulated surface pressure, temperature, and wind speed were precisely adjusted for height variations using the hypsometric equation, lapse rate correction, and logarithmic wind profile, respectively. These height corrections are essential for accurately comparing the model results and the observed data (Deb et al., 2016).

3. Results

3.1. Spatial and temporal precipitation characteristics

The spatial and temporal characteristics of the EPE on November 8 and 9, 2015, over the DML region are depicted in Fig. 1. The figure shows the spatial distribution of daily accumulated precipitation values simulated by the Polar WRF model on November 8 (Fig. 1a) and 9 (Fig. 1b) within the model's 9 km resolution domain. The orography contours (red lines) highlight the complex orographic structure of the coastal region, with closed contour lines indicating areas of significant orographic gradients over short distances. This region has complex orographic features, such as ice rises, steep mountain slopes, and nunataks (Rotschky et al., 2007). The spatial precipitation pattern and orography contours illustrate that precipitation fell predominantly in the coastal and escarpment regions near steep gradient areas. The highest precipitation values were concentrated on the eastern slopes of the orographic features in the near coastal region. The high-resolution analysis using Polar WRF simulated the effect of coastal orography in controlling the spatial distribution of precipitation. The event exhibited a broad spatial coverage spanning 5°W to 20°E and was characterized by significant spatial variability with a number of regional maxima and minima along the coastal region. Spatially, there were three (on November 8) to four (on November 9) peaks of high precipitation values over the region associated with the undulations in the orography of the area. On November 9 (Fig. 1b), there was an eastward shift in the spatial pattern due to the eastward propagation of the cyclonic system and moisture transport conducive to the precipitation event. According to ERA5, November 8, 2015, was the day with the highest precipitation at the ice core location (IND33–71.51°S,10.15°E, Fig. 1) for 1980–2021, with a daily total of nearly 32 mm (fig. S2a). This event contributed approximately 22 % of the 2015 total annual precipitation, based on the 2-day (November 8 and 9) accumulated value. This precipitation event at the IND33 location started at 18:00 UTC on November 7 and ended at 12:00 UTC on November 9, 2015, and the temporal distribution had two peaks of high precipitation rate (Fig. S2b).

Table 1
Parameterization schemes used in Polar WRF model simulation.

Model configuration	Physics scheme/ details
Longwave radiation scheme	RRTMG longwave scheme
Shortwave radiation scheme	Goddard shortwave scheme
Cloud microphysics	Morrison 2-moment scheme
Land surface physics	Unified Noah Land Surface model
Planetary boundary layer physics	MYNN level-2.5 scheme
Surface layer physics	Revised MM5 Scheme
Cumulus parameterization scheme	Kain-Fritsch scheme

For the detailed temporal analysis of the event, we utilized observed variables from the PE station situated slightly inland in DML (Fig. 1a). The hourly precipitation rate from the MRR2 radar at the PE station exhibited episodic and highly variable precipitation values between January 2015 and May 2016. The highest precipitation rate occurred on November 9, 2015, marking the peak within this observed period (Fig. 1c). The temporal precipitation pattern during this event was analyzed using observed hourly precipitation rates and compared with the Polar WRF model outputs and ERA5 values from the nearest grid point to the observation point (Fig. 1d). As the PE station is positioned east of IND33, the snowfall commenced at 09:00 UTC on November 8 and finished at 08:00 UTC on November 10, 2015. Two peaks in the temporal distribution of precipitation were observed at 06:00 UTC on November 9 and 15:00 UTC on November 10, 2015, with precipitation rates reaching up to 2 mm/h (Fig. 1d). These temporal peaks align with the frontal bands approaching these locations, and the Polar WRF model successfully simulated this temporal variability with a good representation of the peaks. There is a slight overestimation of precipitation values in the model on November 11. However, the ERA5 model underestimates precipitation values at the PE station, and the temporal peaks during the event are not well represented (Fig. 1d). To understand the representation of this event in different reanalysis products (JRA55, MERRA2, CFSv2, ERA5), we analyzed their outputs on November 8, 2015 (Fig. S3). All the reanalyses captured the broad-scale intense precipitation amounts and spatial distribution on November 8, 2015, particularly the dominant three-band structure. However, there are differences in the precipitation magnitude across these models, likely due to variations in model resolution and the representation of orography in the complex coastal terrain (Gehring et al., 2022; Mottram et al., 2021). The dynamically downscaled high-resolution regional model, Polar WRF, demonstrated a clear improvement in both spatial and temporal precipitation distribution over the coastal region compared to the reanalyses, highlighting the importance of accurately representing orographic features in these models. The high-resolution simulation using the Polar WRF model showed higher precipitation values than the reanalyses, attributed to its better ability to capture the interactions between steep orographic structures and advected air masses during the event. While reanalysis models are adequate for capturing large-scale interactions, they lack the resolution necessary to resolve highly localized processes in complex terrains like DML. High-resolution regional models, such as Polar WRF, are better suited for simulating snowfall events in these areas, as they can more accurately represent small-scale processes and interactions. The highly variable precipitation distribution, with banded structures, is also evident in climatological precipitation maps over this region (Simon et al., 2024). The complex orography of the region plays a pivotal role in snowfall accumulation and wind-induced redistribution during these EPEs, and the frequency and magnitude of these events can introduce biases in ice-core climate records (Noone et al., 1999).

To examine the temporal evolution of meteorological conditions during the event, we used observed surface meteorological variables from the coastal Antarctic stations Neumayer (Fig. 2a) and Princess Elizabeth (Fig. 2b). We compared these observed variables with the model's nearest grid point values. This analysis demonstrates the accurate representation of surface variables by the Polar WRF model during the precipitation event. The performance of the model's variables was assessed using statistical measures such as correlation, RMSE, and bias (see Table S1). At the PE station, there is a significantly strong correlation between the model and in-situ surface variables such as 2 m temperature (r-value = 0.85), wind speed (r-value = 0.76), and surface pressure (r-value = 0.94). Although there is a slight overestimation of temperature (by 1.5 °C) and wind speed (by 2.7 m/s), the model effectively captured the abrupt changes and temporal variability during the event. Also, the model fails to capture the sudden changes in wind

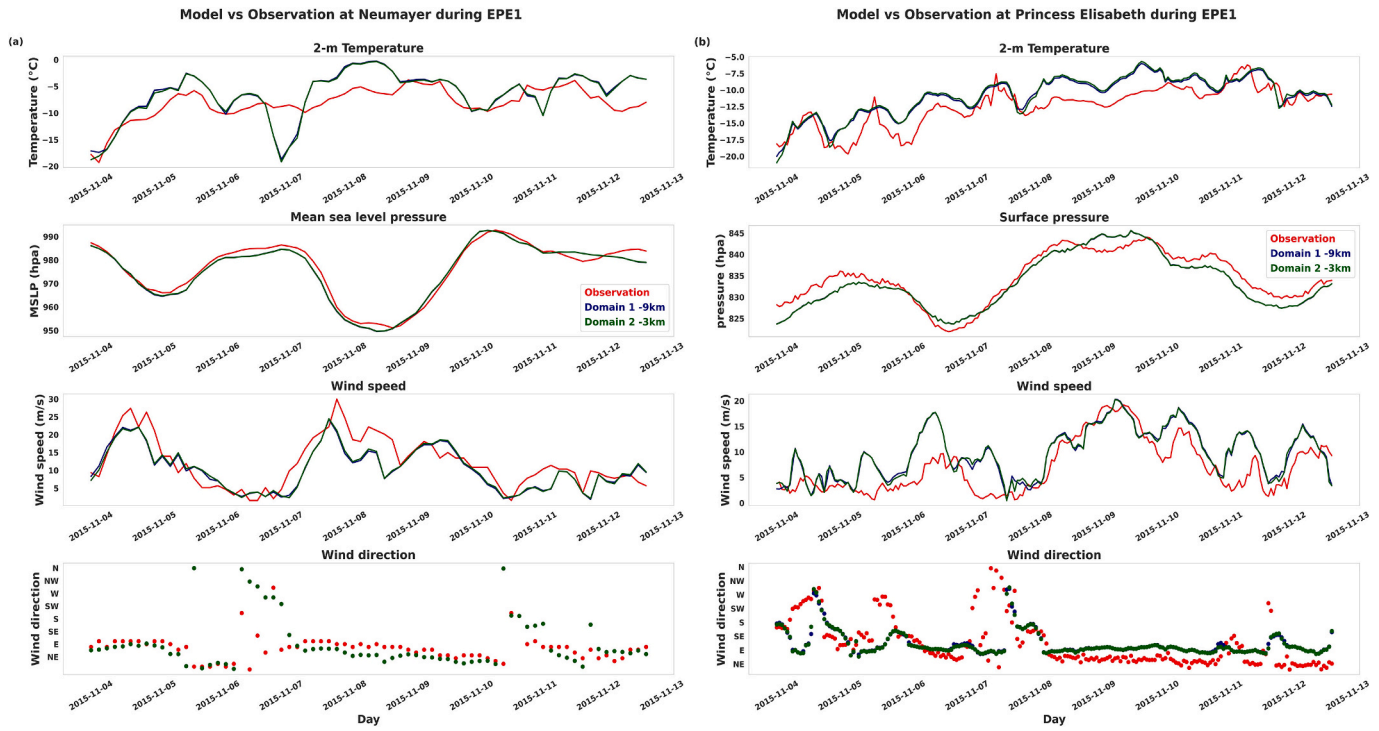

Fig. 2. (a) The validation of the Polar WRF model outputs from both model domains. Time-series comparison of model outputs from the nearest grid point of observed values at Neumayer station for the ten days from November 4 to November 12, 2015. (b) Same as (a), for PE station.

direction from easterlies (E) to north-westerlies (NW) and overestimates the wind speed on November 6 and 7 at the PE station. The comparison with the observed hourly precipitation rate at the PE station shows that the model performed well in capturing the temporal distribution during the event. With a positive correlation of 0.74, the model accurately captures the temporal peaks in the precipitation time series. Overall, there was a slight underestimation (bias ~ -0.04 mm/h) of precipitation values and RMSE values of nearly 0.3 mm/h, and there was an overestimation of precipitation values on November 11. However, considering spatial and temporal changes during this precipitation event, Polar WRF shows a good representation as per the statistics at the PE station and spatial maps. On the other hand, the model underestimated the 2-m temperature at Neumayer station on November 7 and 11, before and after cyclone landfall, as indicated by changes in MSLP values. The model incorrectly simulated the wind direction as NW-N instead of SW-S on November 7, resulting in a sudden temperature drop. Similarly, on November 11, the model misrepresented the wind direction as SW-S instead of SE, contributing to the cold bias. Despite these discrepancies, the model performed well with precipitation at PE and Neumayer stations, as indicated by the model-to-observation comparison statistics (Table S1).

3.2. *Extreme conditions during the event*

To understand the event's unique extreme character and its associated atmospheric dynamics, we employed an extreme value analysis on different atmospheric variables during the event. These variables include MSLP, 500 hPa geopotential height, 10 m wind speed, and integrated water vapor transport (IVT). We marked extreme value points in Fig. 3 to highlight the unique nature of the event. In Fig. 3a, 500 hPa geopotential height values on November 8 exceeded the 95th and 99th percentiles, particularly to the east of DML. This signifies an inland, high-pressure ridge of record strength during the event, which acted as a block for the deep cyclone's eastward progression. Extreme MSLP values below the 5th and 1st percentiles (Fig. 3b) indicate an intensified low-pressure system west of the region, progressing southeastward from the South Atlantic Ocean and landfall on November 8. Daily averaged MSLP values show a pronounced depth recorded at the center of this low-pressure cyclone. These extreme, free atmosphere and lower troposphere conditions initiated strong northerly winds and intense moisture transport towards Antarctica (Fig. 3c, d). The combination of a low-pressure system to the west and a blocking high-pressure ridge to the east is identified as the major synoptic pattern during the EPEs over coastal Antarctica (Welker et al., 2014; Yu et al., 2018). A convergent wind structure is exhibited over the coastal region (nearly 15°E to 30°E), with the presence of katabatic winds from inland regions (Fig. 3c), which leads to the interplay of the warm-moist airmass, cold katabatic winds, and complex orography of the coastal region. IVT values were of intense magnitude on the cyclone's eastern flank and high values over the Atlantic Ocean near 30°S, extended as an atmospheric river towards Antarctica (Fig. 3d). This AR on November 7 and 8, 2015 was one of the strong AR events identified at IND33 with maximum IVT values greater than the 99th percentile values of all ARs occurrence at this location. The ARs at IND33 were tracked and found using the AR detection criteria of Wille et al. (2021). A detailed analysis of this AR is explained in section 3.5.

Extreme precipitation and temperature values during and following the landfall of an AR are comprehensively shown in Fig. 4. Most coastal areas exceeded the 95th percentile precipitation threshold and experienced snowfall extending inland on November 9, concurrent with the intrusion of a blocking ridge. Simultaneously, 2 m temperatures displayed extreme values on November 9 and 10 (Fig. 4c, d), propagating inland post-event. As part of the detailed analysis, atmospheric thickness (1000–500 hPa) was examined throughout the event (Fig. S4), which depicted the heat content of the lower troposphere. On November 6, a northward extension of the trough region around 30°W indicated the movement of cold air from polar to low latitudes, reflected in lower thickness values. The inland extension of high thickness values on November 7 and 8 demonstrated the advection of warm air towards the ice sheet, particularly over 0–30°E, resulting in higher temperatures. This warm air advection was associated with the intrusion of a high-pressure ridge into the inland region. Surface heat fluxes during the

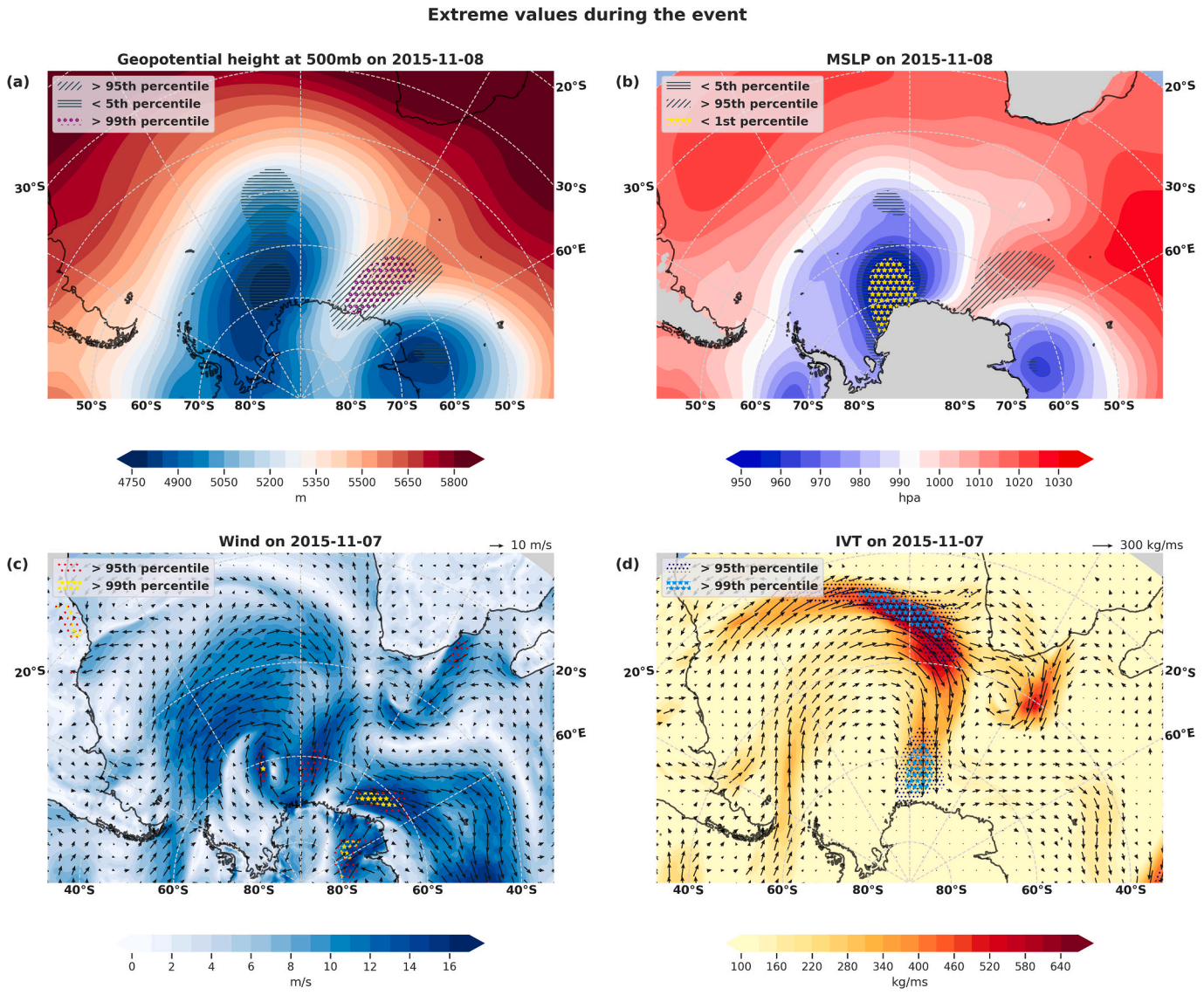

Fig. 3. Synoptic conditions during the precipitation event in the ERA5 model and the regions with extreme values found using percentile criteria are denoted in the figure. (a) geopotential height at 500mb, (b) Mean Sea Level Pressure, (c) Wind speed at 10 m, (d) Integrated water vapor transport (IVT). The percentiles are calculated using daily data from ERA5 for the 1979–2018 period. The MSLP values over the high-altitude regions are masked.

event in this high-temperature area (averaged over 5°E-35°E, 71°S-83°S, the selected box marked in Fig. 4c, d) revealed hourly changes in radiative and turbulent heat fluxes (Fig. S5). Longwave (LW) radiation values (w/m^2) were less negative during the event, indicating downward LW radiation from clouds. Warmer conditions during the event also caused decreased heat loss from the ice sheet to the atmosphere. Clouds over the ice sheet reflected incoming solar radiation, decreasing net short-wave radiation values. Consequently, warm airmass and clouds above the ice sheet surface resulted in a downward (more positive) surface sensible heat flux during the event. This demonstrates the warming due to cloud-longwave radiation and associated sensible heat fluxes contributing to changes in net radiation, primarily when 2 m temperatures increased sharply by nearly 15 °C in less than 36 h (from 01:00 AM on November 8 to 10:00 AM on November 9). The reported warmings over the Antarctic ice sheet in several studies (Turner et al., 2022; Wille et al., 2023) is primarily attributed to the advection of warm airmasses causing cloud formation upon interacting with the complex orography of the region and changes in longwave radiation from the atmosphere to the ice sheet. Large-scale features, such as the presence of blocking high-pressure regions with sinking air motion and local features like downslope foehn winds from high orographic areas, can lead to sudden changes in atmospheric temperature and warming over the ice sheet (Gorodetskaya et al., 2023; Zou et al., 2022).

3.3. Genesis and movement of the mid-latitude cyclone

Fig. 5 illustrates the MSLP values and 500 hPa geopotential height during and preceding the precipitation event. The synoptic processes behind this event were initiated on November 4. On that day, the area north of the Weddell Sea was characterized by multi-centered, quasi-stationary, low-pressure systems and the generation of a highly amplified zonal wave pattern north of DML in the circumpolar trough (40°S - 60°S). On November 5, the mid-troposphere had an upper-level short wave trough over the Weddell Sea sector (nearly 57°S, 15°W). This shortwave trough initiated the cyclogenesis, and as a result, a low-pressure system deepened near 55°S, 5°W in the South Atlantic Ocean on November 6. On November 7, this system underwent rapid deepening, with the lowest central pressure being nearly 951.8 hPa. In parallel with the deepening (on November 8, the lowest central pressure reached up to 941.4 hPa), this cyclone tracked poleward and made

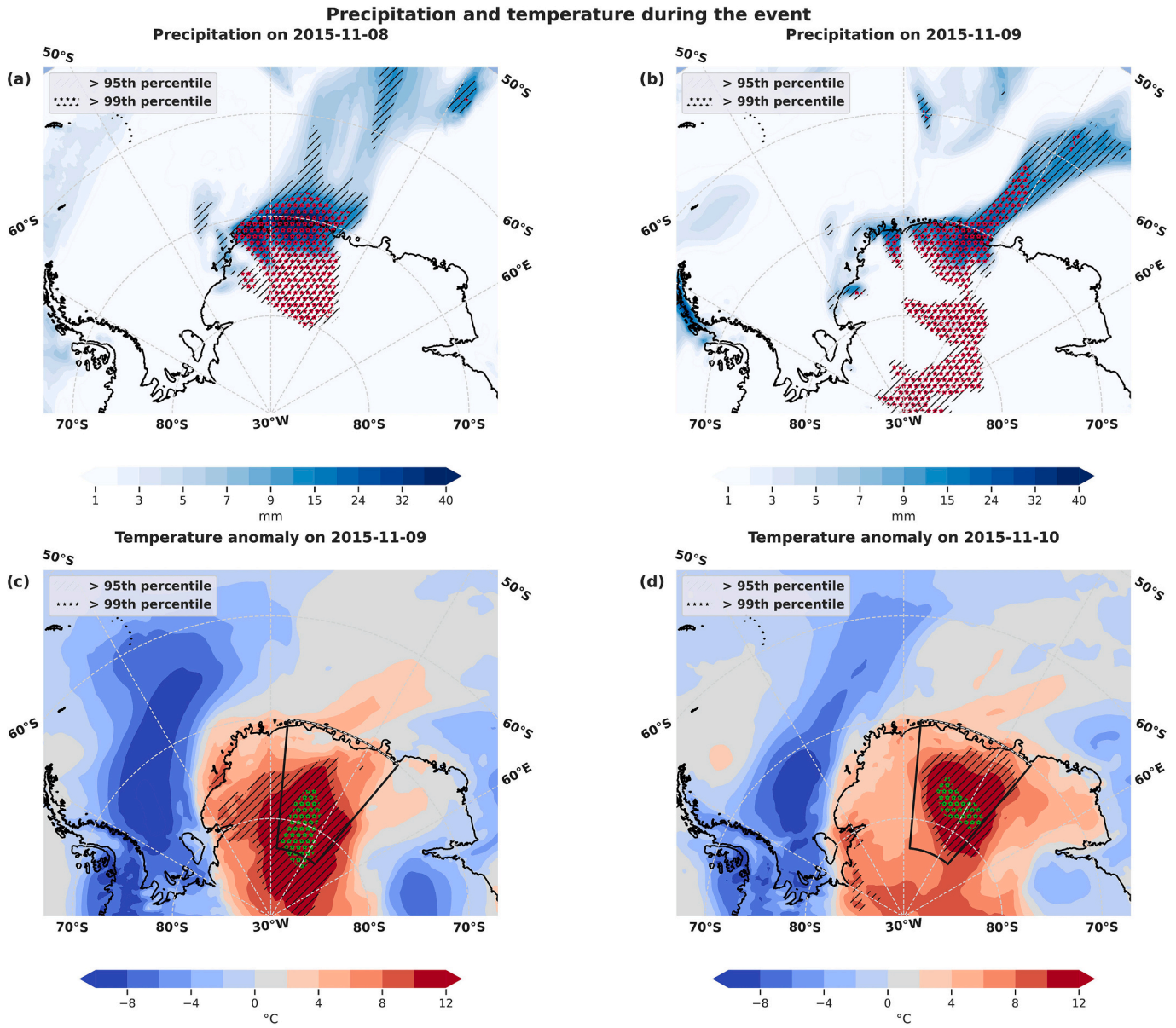

Fig. 4. Similar to Fig. 3, regions showing extreme values were found using percentile criteria (a) daily precipitation values during November 8, (b) daily precipitation values during November 9, 2015, (c) 2-m temperature anomaly values during November 8, (d) 2-m temperature anomaly values during November 9, 2015. Daily anomaly values were calculated using data for the climatology period 1979–2018. The box selected for temporal analysis of radiative and turbulent flux values is also marked in (c) and (d).

landfall on the DML coast on November 8. The MSLP exhibited a prominent zonal wave number 3 pattern, with low-pressure systems located at 145°W, 120°E, and 5°W during the first week of November 2015. Between November 7 and 8, a high-pressure ridge of record strength developed east of the region, redirecting the low and facilitating substantial moisture transport towards the region. The 500 hPa geopotential height shows the extensive amplification of the planetary wave pattern in the mid-tropospheric north of the region, forming a high-pressure blocking ridge to the east. The sudden deepening of the low and the inland extension of the blocking ridge on November 7 and 8 served as the primary mechanisms steering the surface low towards land, generating a prolonged and narrow moisture pathway as an intense atmospheric river.

The extra-tropical cyclogenesis on November 7 occurred within the frontal boundary of warm and cold air masses. The frontal zones of large horizontal temperature gradient were on the eastern side of the surface low, and the interaction of warm and cold air over this boundary helped cyclogenesis. The 850 hPa potential temperature and gradient of 850 hPa wet-bulb temperature from the Polar WRF model (Fig. S6b, S6c) confirm the frontal zones. The rising warm air over the frontal boundary led to the thick cloud on the eastern flank of the cyclone. The satellite images at the time of the event (Fig. 6) also confirm the presence of a long band of cloud and moisture through the eastern side of the cyclonic system (Fig. S6a). Fig. 6 shows the typical cloud band structure of an AR propagation with intense moisture from low-latitudes towards coastal Antarctica. These satellite images show the frontal cyclogenesis occurred during the event, and the poleward movement of warm low-latitude air and the northward movement of cold inland air led to the forming of a frontal boundary near the low's center and the system's deepening as it moved southwards (Fig. 6). The inland extended high-pressure ridge supported the movement of cold air from the interior of the continent, which also contributed to the sudden strengthening of the low-pressure cyclone by increased baroclinicity. Francis et al. (2021) also reported similar interactions of the inland high-pressure systems

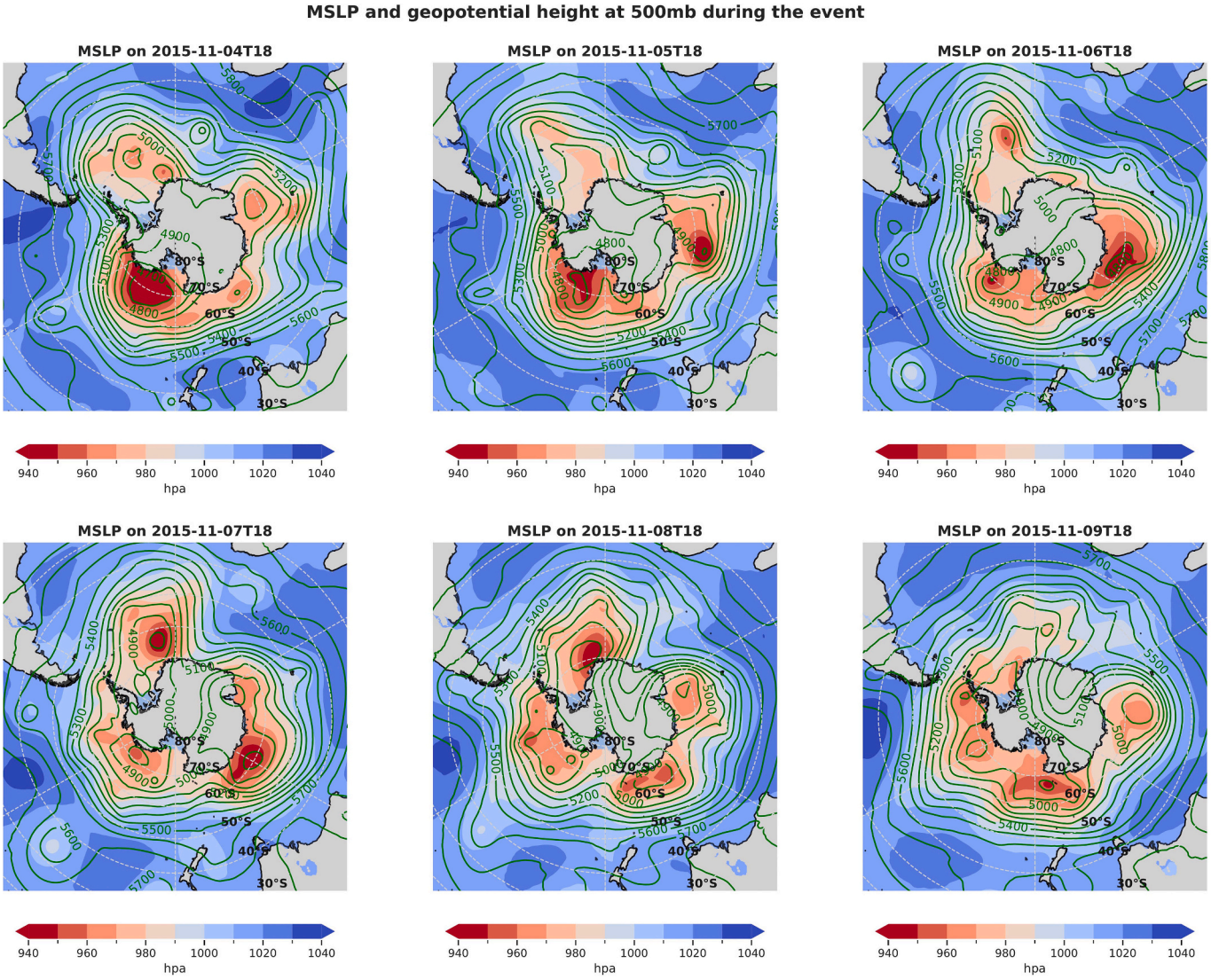

Fig. 5. The mean sea level pressure (MSLP) values (shaded, unit (hPa)) overlaid by geopotential height at 500 hPa (green lines, unit (m)) at the 18th hour six consecutive days before and during the event. (For interpretation of the references to colour in this figure legend, the reader is referred to the web version of this article.)

causing the strengthening of cyclones over the Southern Ocean by the advection of cold interior air. The landfall of the cyclone over DML on November 8 is also verified by the satellite images, with clouds extending well into the inland in consecutive hours.

3.4. *Upper-level winds and steering mechanisms*

To identify the influence of upper-level dynamics and wind patterns in the propagation and occurrence of this event, we analyzed the atmospheric flow at 250 hPa. Fig. 7 shows the 250 hPa wind and geopotential height from November 5 to 10, at 18:00 UTC. The upper-level winds show the highly amplified zonal wave near the 50°S - 60°S circle with the genesis of the inland-extending high-pressure ridge north of DML. A prominent quasi-stationary trough and ridge pattern started developing near 10°W on November 5 and amplified before the extreme precipitation days of November 8 and 9, 2015. The inland intrusion of a high-pressure ridge is evident from the upper-level geopotential height values, accompanied by changes in wind direction. This anomalous inland intrusion of the ridge, associated with the blocking mechanism, was the main feature responsible for redirecting the strong cyclone and high moisture levels to the landfall region (Fig. 4). Notably, there was a close interaction between the subtropical and amplified polar jet streams north of the Weddell Sea (30°S, 20°W), where strong moisture uptake occurred (section 3.5). On November 6 and 7, the upper-level trough exhibited strong meandering. It extended poleward, facilitated by a narrow band of strong meridional wind known as a 'jet streak' in the upper atmosphere, particularly over 10°W to 5°E. The core of this jet streak was on the eastern side of the upper-level trough and extended southward before the event. A cross-section analysis of this strong wind region during the event confirms this wind band's formation and poleward extension (Fig. 8). The meridional wind, averaged across longitudes 5°W to 10°E, is depicted in Fig. 8. The strengthening and formation of the jet streak occurred on November 6 and 7, generating a band of strong meridional wind over the 50°S to 70°S at 18:00 UTC on November 7. The core of this strong southward wind was close to 300 hPa, reaching coastal Antarctica on November 8, and interacted with coastal orographic features (Fig. 8). These strong upper-level winds led to upper-level divergence balanced by the lower-level convergence and enhanced vertical motion. The vertical motion led to the deepening of the low-pressure system, and upper-level winds steered the system southwards. Therefore, the meridional jet streak in the upper atmosphere played a significant role in the sudden deepening of the low-

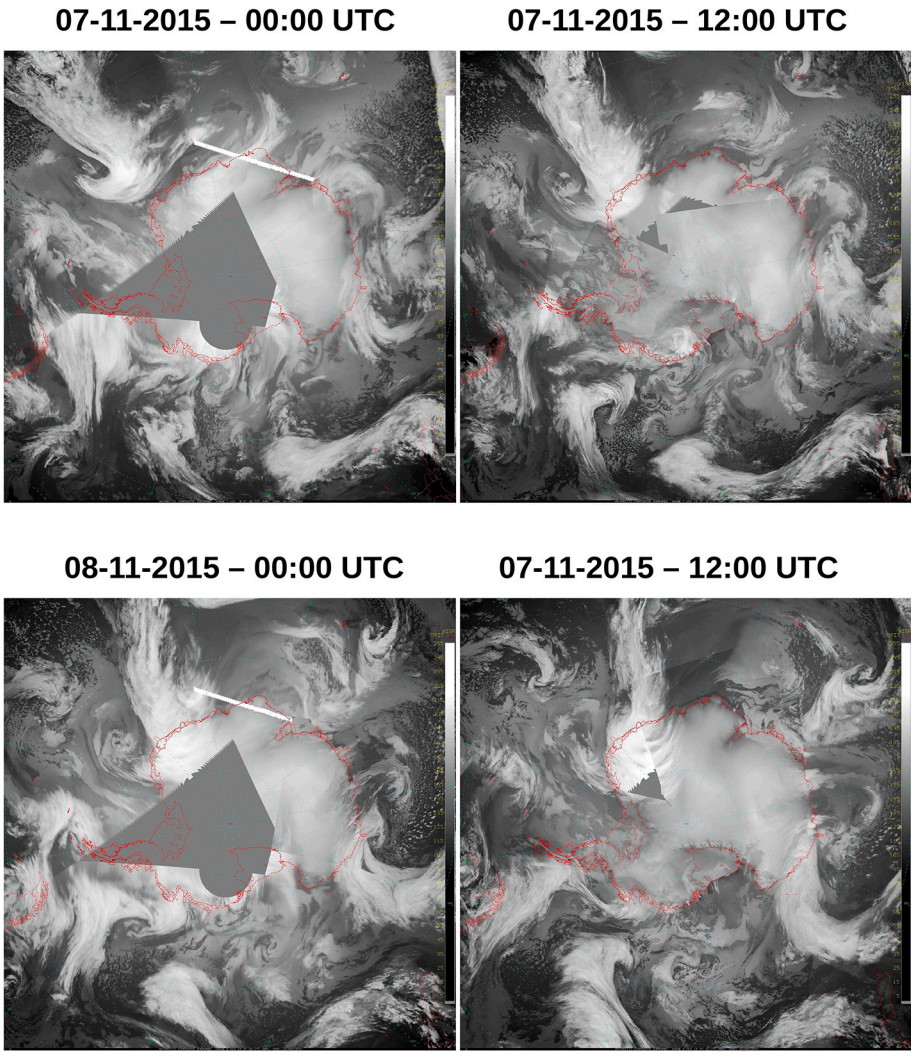

Fig. 6. Infrared satellite imagery (IR) (~11.0 μm) for the different hours before and during the event.

pressure system and warm, moist airmass advection on November 7. On November 8, this band of strong wind reached coastal Antarctica associated with the landfall of the cyclone.

The Hovmöller (time vs. longitude) diagram in Fig. S7 illustrates changes in the zonal and meridional 250 hPa wind components averaged from 40°S to 70°S between November 1 and 12, 2015. The meridional wind (Fig. S7a) revealed alternating strong winds from the south (positive values) to the north (negative values) over the circumpolar trough region (Fig. S7a, dashed line), beginning around 180°W on November 1. This oscillation gradually propagated eastward over time, with significant northerly winds near 130°W on November 2 and 10°E on November 7. This signifies the downstream movement of the Rossby waves, forming two strong ARs over these zones (130°W and 10°E). The AR near 10°E was linked to the extreme event over DML, with a meridional jet streak causing strong northerly winds. The zonal winds (Fig. S5b) exhibit strong westerlies in the South Atlantic and Indian Ocean (30°E to 150°E) during the initial week of November. However, from November 7 to 10, zonal winds weakened in the Weddell Sea and South Atlantic (30°W to 60°E) due to prevailing northerly winds and their eastward advancement. Simultaneously, the Ross Sea sector (180°W to 90°W) experienced strong zonal winds. The upper-level winds reveal a semi-stationary wave pattern in the north-south flow, with changes in the wind pattern attributed to amplified planetary waves during the EPE days. The intensified Rossby wave pattern and the associated meridional jet streak in the upper atmosphere played a significant role as the primary steering mechanism. This aligns with the findings of Wang et al. (2023), supporting the idea that the intensification of Rossby waves in the circumpolar region can trigger the genesis of intense blocking activity and precipitation events in East Antarctica.

3.5. *Moisture transport associated with AR*

Hourly IVT fields associated with intense moisture transport in the form of AR and the development of the deep cyclonic system in 6-hour intervals from 18:00 UTC on November 6, 2015, are depicted in Fig. 9. A pool of high IVT values, about 1000 kg/ms, was present over the South Atlantic (the 30°S - 40°S, 30°E - 5°E) ocean on November 6. This region coincided with the northern end of the amplified upper-level trough (explained in section 3.4) interacting with the sub-tropical jet stream where strong moisture uptake occurred (Fig. 10). The moisture transport was strengthened and started to orient meridionally on November 7, associated with the strengthening of the blocking high-pressure ridge to the east and deepening of the low to the southwest. This quasi-stationary atmospheric pattern helped in the poleward movement of moisture and the formation of an AR that elongated southward along the eastern flank of the extra-tropical cyclone. To investigate the vertical structure of IVT, we included the cross-section analysis of moisture flux for the entire vertical atmospheric column along the eastern flank and warm sector of the surface low (averaged between longitudes 5 W to 10E), as depicted in Fig. 10. The contours of specific humidity (violet) are overlaid. At

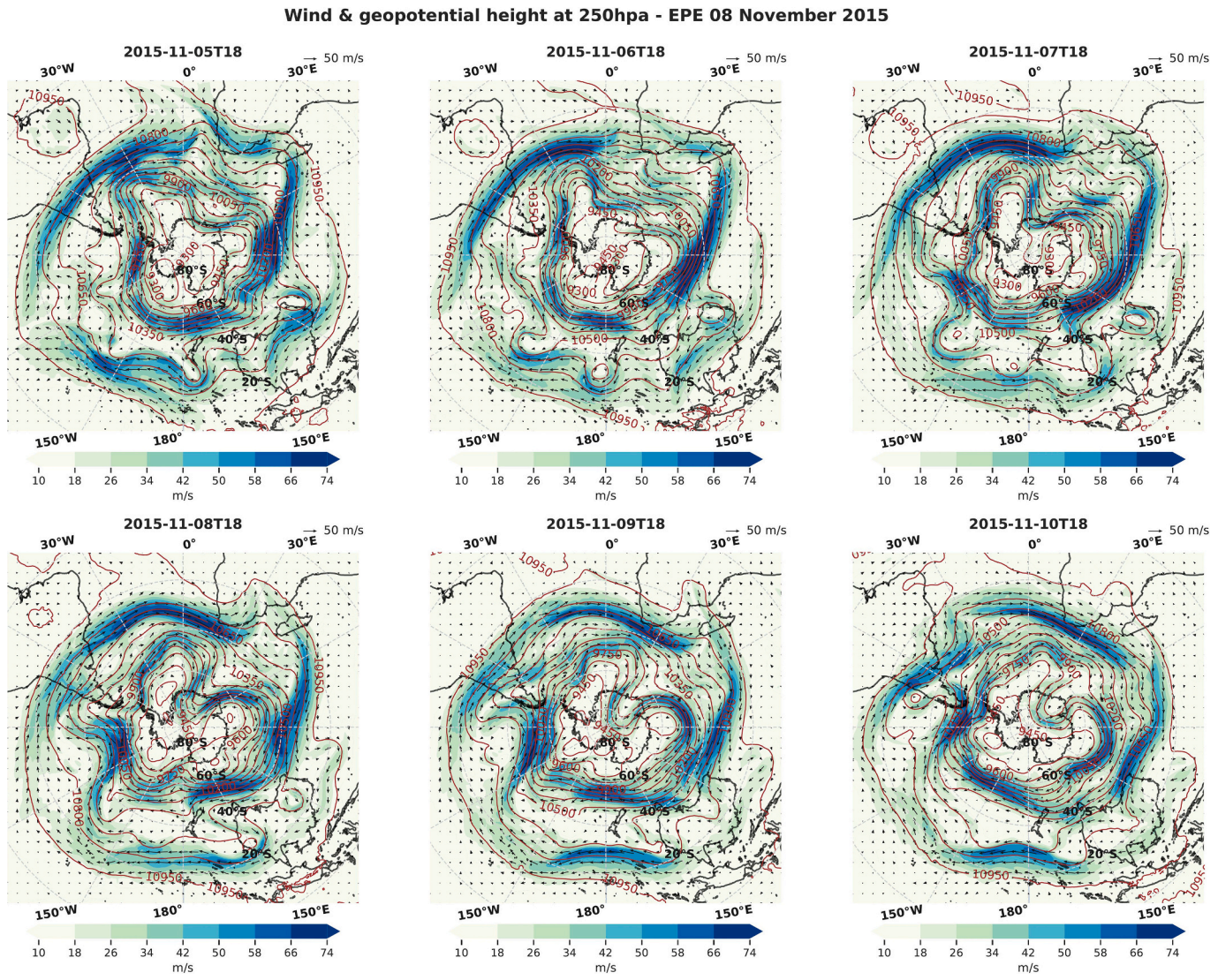

Fig. 7. Wind speed (shaded, units (m/s)), wind vectors, and geopotential height (brown lines, units (m)) at 250 hPa for different hours before and during the event. (For interpretation of the references to colour in this figure legend, the reader is referred to the web version of this article.)

18:00 UTC on November 6, large areas of enhanced moisture flux on the northern end (nearly 30°S to 40°S) of the cyclone. Enhanced moisture flux values over this region on November 7 in the lower troposphere (750 hPa to 950 hPa) were mainly controlled by high specific humidity values and termed the major moisture uptake region. The meridional orientation of this moisture pool took place throughout the remaining hours of November 7 with the support of upper and lower-level winds. The moisture flux had high values from 300 hPa to the surface. These plumes of intense moisture were heterogeneous over the lower troposphere and became two major bands of moisture flux over 60°S and 38°S at 12:00 UTC on November 7. This two-band structure is also reflected in the coastal region's temporal distribution of precipitation at point locations (PE station, IND33 - Fig. 1d, Fig. S2b). The poleward orientation and eastward movement of this long, narrow band of moisture were largely driven by the deepening and eastward movement of the low-pressure system, which made landfall over the coastal region on November 8. The highly amplified zonal wave and blocking ridge contributed to the moisture transport into the coastal region associated with the cyclone's landfall. The AR formation and meridional elongation of high moisture flux occurred within 24 h, which closely aligns with the sudden deepening of the low-pressure cyclone in the Atlantic Ocean steered by the upper-level winds. The onset of precipitation in the early hours of November 8 coincided with the interaction of these intense moisture bands with the orographic features of coastal DML.

3.6. Orographic enhancement

On November 8, 2015, as previously discussed, coastal precipitation peaked due to the cyclone's landfall and the arrival of an atmospheric river from the South Atlantic Ocean. The region also experienced winds from the N-NE direction, which advected warm, moist air from northern latitudes. There is high precipitation over the oceanic region just north of the DML coast, which is due to the interaction of warm airmass with cold air from the continent inland. This interaction enhanced the rapid cooling, condensation, and precipitation near the coastal margins and over coastal ice shelves. The precipitation values over the ice sheet were of record magnitude in most coastal DML. However, the distribution of precipitation values was not homogeneous, and there was high spatial variability along the coast, showing a three-band pattern of high and low values (Fig. 11a). We utilized results from Polar WRF simulated on high precipitation days for a better understanding of this high spatial variability with bands of high and low precipitation values. To accurately capture key orographic and small-scale processes over the coastal region, we used outputs from a high-resolution model domain (3 km). We

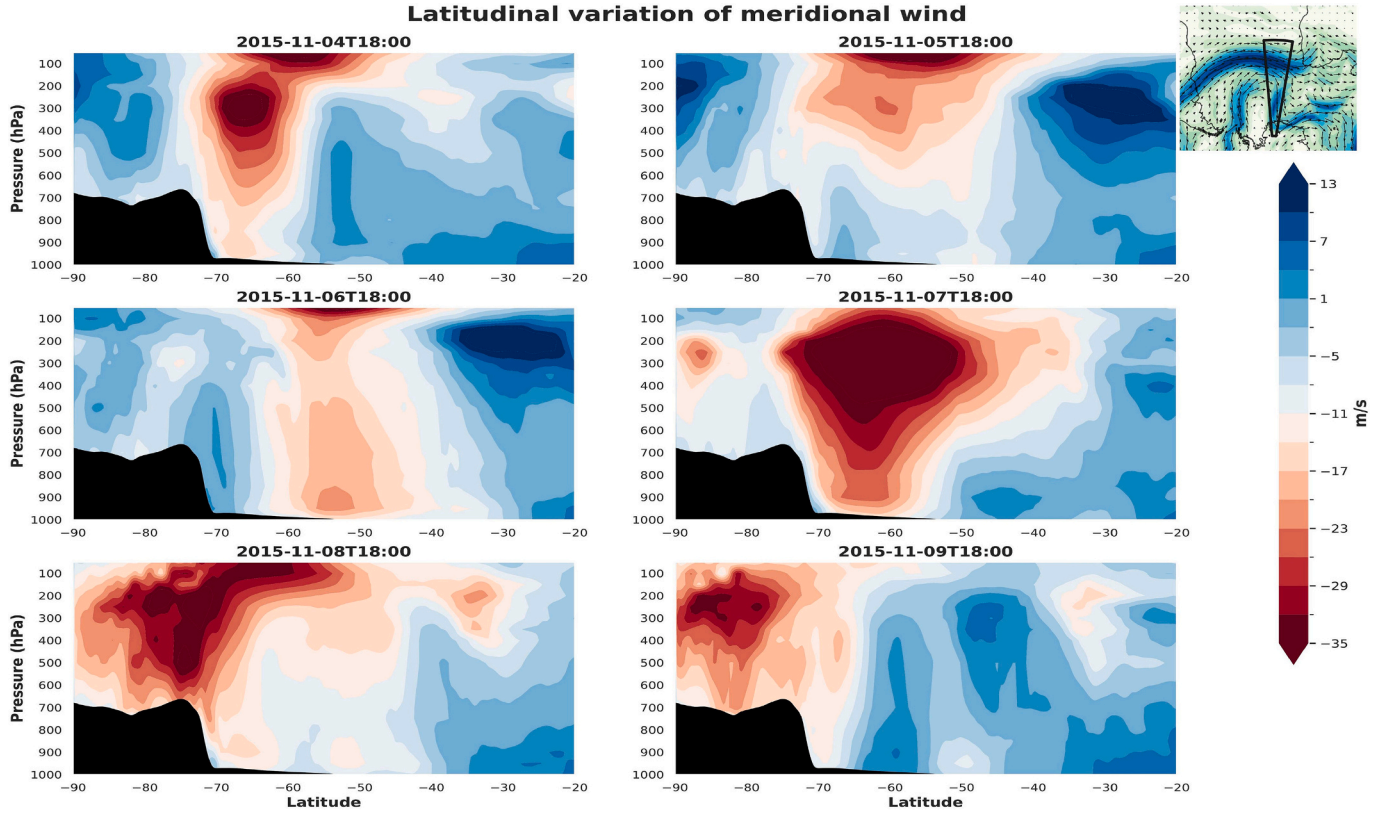

Fig. 8. Vertical cross-section analysis of v-component of wind (shaded, unit(m/s)) averaged through the jet streak area (5°W to 10°E) for different times before the event. The insert shows the location of the respective cross-section (black box) relative to the wind speed (shaded) and wind direction (vectors). See Fig. 7.

focused on analyzing the vertical distribution of atmospheric variables during the event, selecting a west-east oriented plane that highlighted significant spatial variability in precipitation. (Fig. 11a). The cross-section captures the complex orography of the coastal region with the vertical variation in variables such as omega, mixing ratio of water vapor and snow, relative humidity, and moisture flux (Fig. 11b, c, d, e, f) at 12:00 UTC on November 8, 2015, when hourly precipitation reached its peak. The orography of the region is complex, with steep slopes over a short distance due to mountain regions, nunataks, and ice rises. The synoptic patterns confirm the intense moisture transport in the form of ARs reaching the coastal region on November 8 (Fig. 9). The interaction of warm, moist airmass with the orography of the region is illustrated in the vertical cross-section analysis, where Fig. 11b shows the omega (pa/s) values with wind vectors showing vertical wind directions. The effect of coastal orography is evident in the vertical distribution of omega (pa/s) values along this selected cross-section zone (Fig. 11c). Alternative positive and negative omega values were present over the lower troposphere, and significant negative values near the steep gradient zones (Fig. 11c). The negative omega values indicate strong vertical motion of air parcels, which results in the orographic lifting and cooling, leading to enhanced precipitation over these windward regions. The regions with high precipitation values are near steep, complex terrain with strong updrafts, especially near the 5°W, 5°E, and 10°E. Alternate downdrafts, with relatively lower moisture content, balance these strong updrafts, resulting in minimum precipitation values. The vertical wind vectors confirm this rapid updraft and downdraft pattern in the lower troposphere and indicate the close interaction of advected airmass with the complex orography of the region. The presence of alternating updraft-downdraft wind regions associated with the complex coastal orography was also demonstrated by Gehring et al. (2022), which explains the role of foehn winds and lower troposphere sublimation in creating low precipitation bands along the coast (Gehring et al., 2022). The cross-section of mixing ratio values of both water vapor (Fig. 11c) and snow (Fig. 11d) shows the distribution of moisture in different levels along the selected plane. The mixing ratio of water vapor shows the moisture advection in the lower atmospheric levels between 2000 m to 4000 m above sea level. This indicates the strong moisture associated with the AR in the lower troposphere, from the northeast region of DML. The near-surface and steep orographic regions show low values in the water vapor mixing ratio, complemented by high values of snow mixing ratio (Fig. 11d), indicating the snowfall formation upon interacting with the orographic features. The snow mixing ratio has a distinct three-band structure with high values in the vertical distribution near the steep gradient terrain regions. This is in close agreement with the snowfall distribution pattern on November 8, 2015 (Fig. 1a, 11a), with high values near the windward side of coastal orographic features. Similarly, the lower atmosphere had distinct vertical columns of high moisture content with 3–4 bands of completely saturated areas (RH = 100 %) (Fig. 11e). These highly saturated areas are also near the steep-gradient orographic features along the line of cross-section analysis. The derived high moisture flux regions (Fig. 11f) also correspond to the coastal high precipitation bands. These moisture-rich zones align with steep-gradient orographic areas oriented perpendicular to the N-NE winds during the event. Hence, peak precipitation values were on the windward side of these gradients, while the leeward side experienced minimal values. The precipitation bands over the coastal region during this EPE event were associated with the four zones of high moisture flux values due to the orographic enhancement of winds and moisture upon reaching the coast. The vertical distribution of different variables along the selected cross-section highlights the interaction of airmass advected from the oceanic region with the complex coastal orography. This also indicates that despite considerable moisture transportation to coastal Antarctic areas, heavy precipitation was focused on specific locales, notably the windward side of steep orographic features, and implies that the precipitation distribution depends on the orientation of the coastal orography.

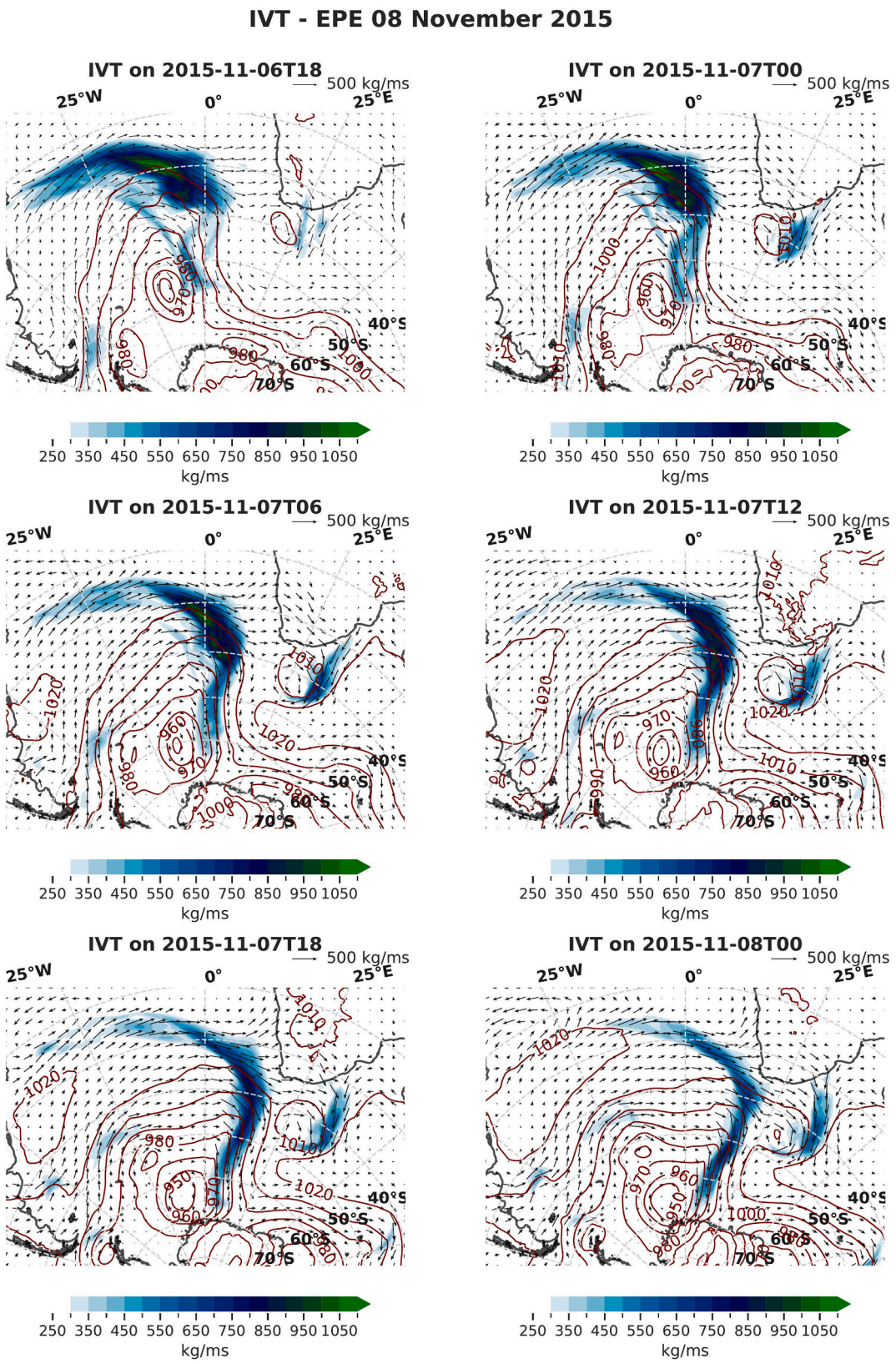

Fig. 9. Temporal evolution of ARs along coastal Antarctica, showing vertically integrated vapor transport (IVT) (shading, units (kg/ms)), moisture transport direction (vectors), and sea level pressure (brown lines, units (hPa)) for 6-hly intervals before the precipitation event. (For interpretation of the references to colour in this figure legend, the reader is referred to the web version of this article.)

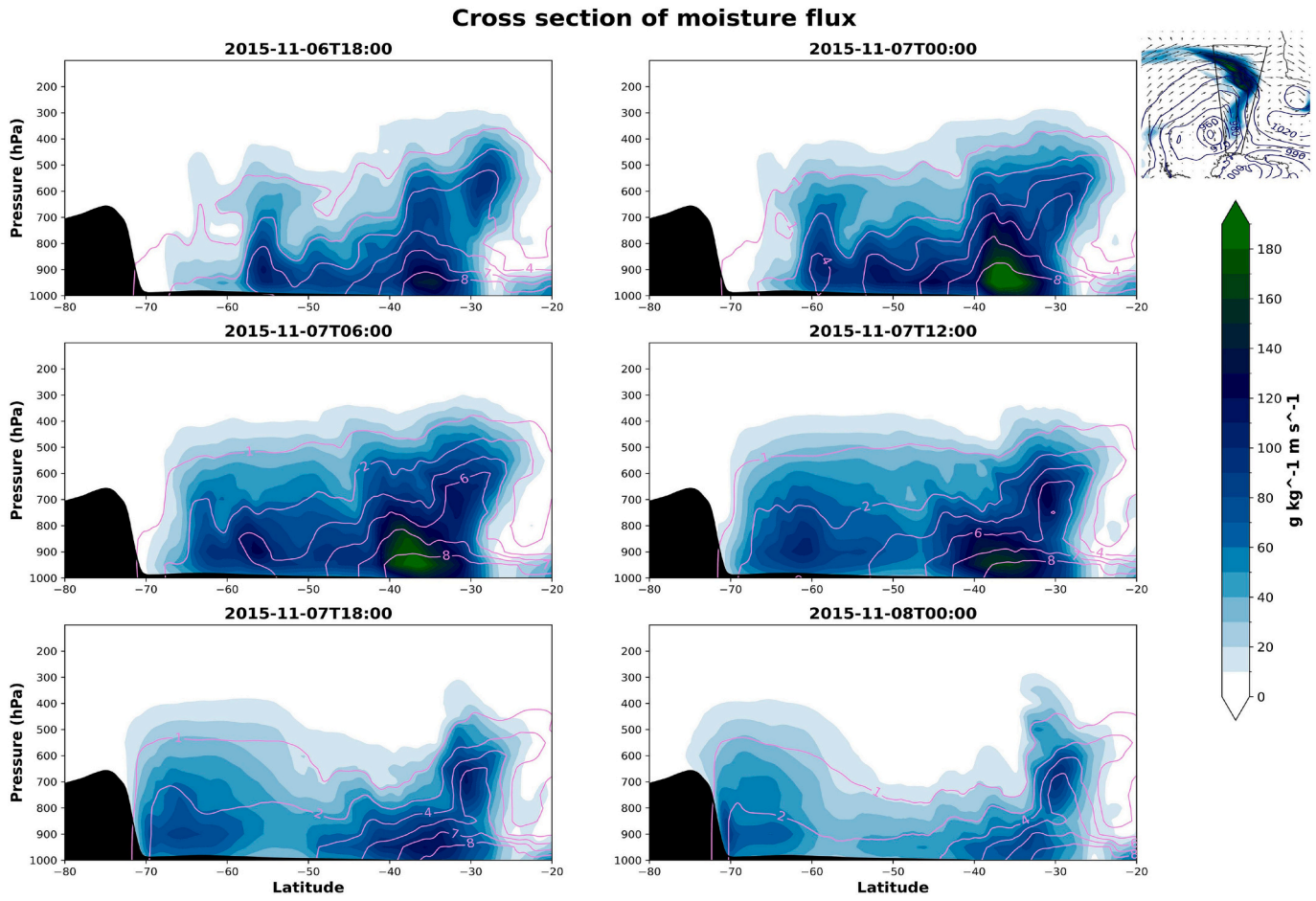

Fig. 10. Vertical cross-section analysis of moisture flux (shaded, unit(g/kg*m/s)) and specific humidity (violet lines, units(g/kg)) averaged through the eastern flank of the cyclone (5°W to 10°E) for different times corresponds to Fig. 9. The insert shows the location of the respective cross-sections (black box) relative to the IVT (shaded), sea level pressure (brown lines), and IVT vectors. See Fig. 9. (For interpretation of the references to colour in this figure legend, the reader is referred to the web version of this article.)

3.7. The long-term significance of EPEs and associated ARs at the ice core location

The EPE on November 8 and 9, 2015, showed an extreme nature in the distribution of snowfall, with large amounts of snowfall within a short time period. Similar to this case, the long-term occurrence and significance of EPEs at the ice core location (IND33) are identified from 1980 to 2021 using the distribution of the largest EPE that occurred each year. Fig. 12 highlights the largest EPE each year, showing its contribution (from three-day accumulated value) to the annual total at the ice core location (IND33) over coastal DML. It also identifies AR and non-AR moisture transport patterns during these events, ranking them by their maximum IVT values. The November 8 and 9, 2015 event stands out as the highest precipitation event among all years between 1980 and 2021, contributing about 22 % of the total annual precipitation. This EPE is associated with a strong AR, which ranks in the top 1 % of all ARs at this location, related to extreme upper and lower atmospheric conditions. In other years, the single, largest precipitating event even contributes approximately 10–20 % of the annual precipitation, with significant interannual variability.

Years with AR occurrences are notable for high precipitation values, and during these high-magnitude EPEs, AR-type moisture transport is present in about 30 out of 41 years. Ranking these events by maximum IVT values reveals that most AR occurrences are within the top 25 % of events, especially for the years in the last decade (2009 to 2021). Recent studies at this same ice core location have observed an increasing trend in the magnitude of precipitation but without any trend in the number of EPE days (Simon et al., 2024). This suggests that more moisture has been transported to coastal regions in recent years, resulting in high-magnitude precipitation over a short period. Long-term climatological studies on DML also indicate that EPEs contribute 50–60 % of the total annual precipitation within just 10–15 days each year, significantly influencing the interannual variability of precipitation, particularly in coastal areas (Simon et al., 2024; Turner et al., 2019). Precipitation from EPEs varies spatially, with ARs playing a key role, contributing approximately 40–50 % of EPEs over DML (Simon et al., 2024; Wille et al., 2021).

As precipitation is the primary input for net surface accumulation, the extreme nature of these high-magnitude events is important while considering ice core records from these regions, as these EPEs can skew isotope records in ice cores to particular seasons or events. Also, the significant changes in surface meteorological conditions during EPEs can cause elevated temperatures and snowfall redistribution due to strong winds. Increased AR occurrences and long-range moisture transport from warm sub-tropical and tropical latitudes also impact the stable isotope records from coastal regions. Additionally, these EPEs can impact surface mass balance and surface temperatures, causing surface melting and potentially mitigating short-term sea level rise.

4. Discussion and conclusions

In this study, we investigated the occurrence of an EPE over DML on

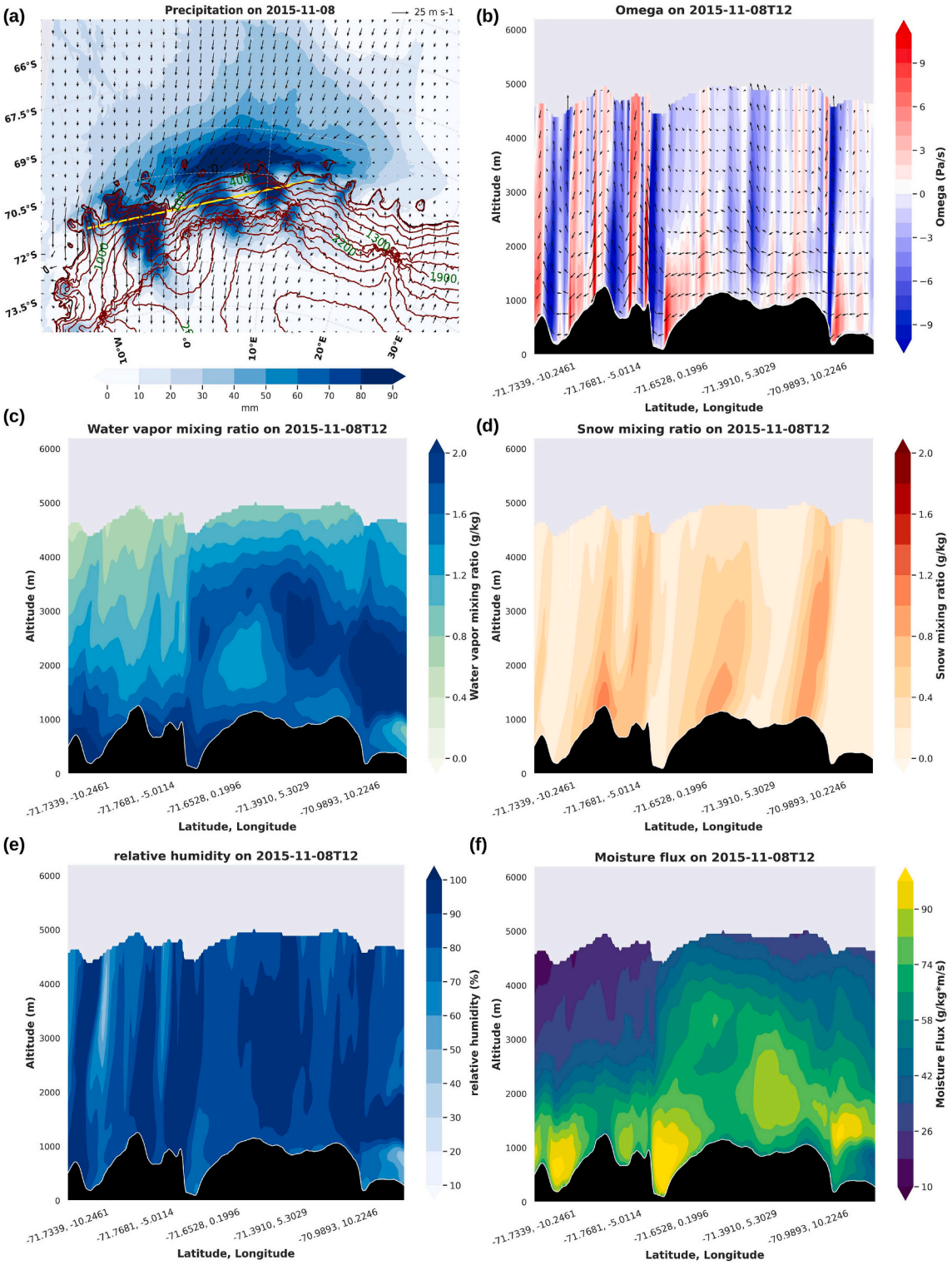

Fig. 11. (a) Similar to Fig. 1a. The area selected for vertical cross-section analysis is denoted with a yellow line. Vertical distribution of variables at 12:00 UTC of November 82,015 over coastal DML from Polar WRF model output from the inner domain of 3 km resolution (b) Omega (unit (pa/s)), (c) Water vapor mixing ratio (unit (g/kg)), (d) Snow mixing ratio ((unit (g/kg)), (e) Relative humidity (unit (%)), (f) Moisture flux (unit (g/kg*m/s)). (For interpretation of the references to colour in this figure legend, the reader is referred to the web version of this article.)

November 8 and 9, 2015. This was the highest precipitation event at one of the coastal ice core sites (IND33). We also shed light on the role of orography during the landfall of an atmospheric river and extreme upper and lower atmospheric conditions.

The event was triggered by a deep low-pressure system moving southwards from the South Atlantic, which was affected by a high-pressure ridge of record strength to the east. The interaction between these extreme low and high-pressure systems generated a strong AR originating over the South Atlantic Ocean across the 30°S to 40°S. This atmospheric pattern was critical to high precipitation events in DML.

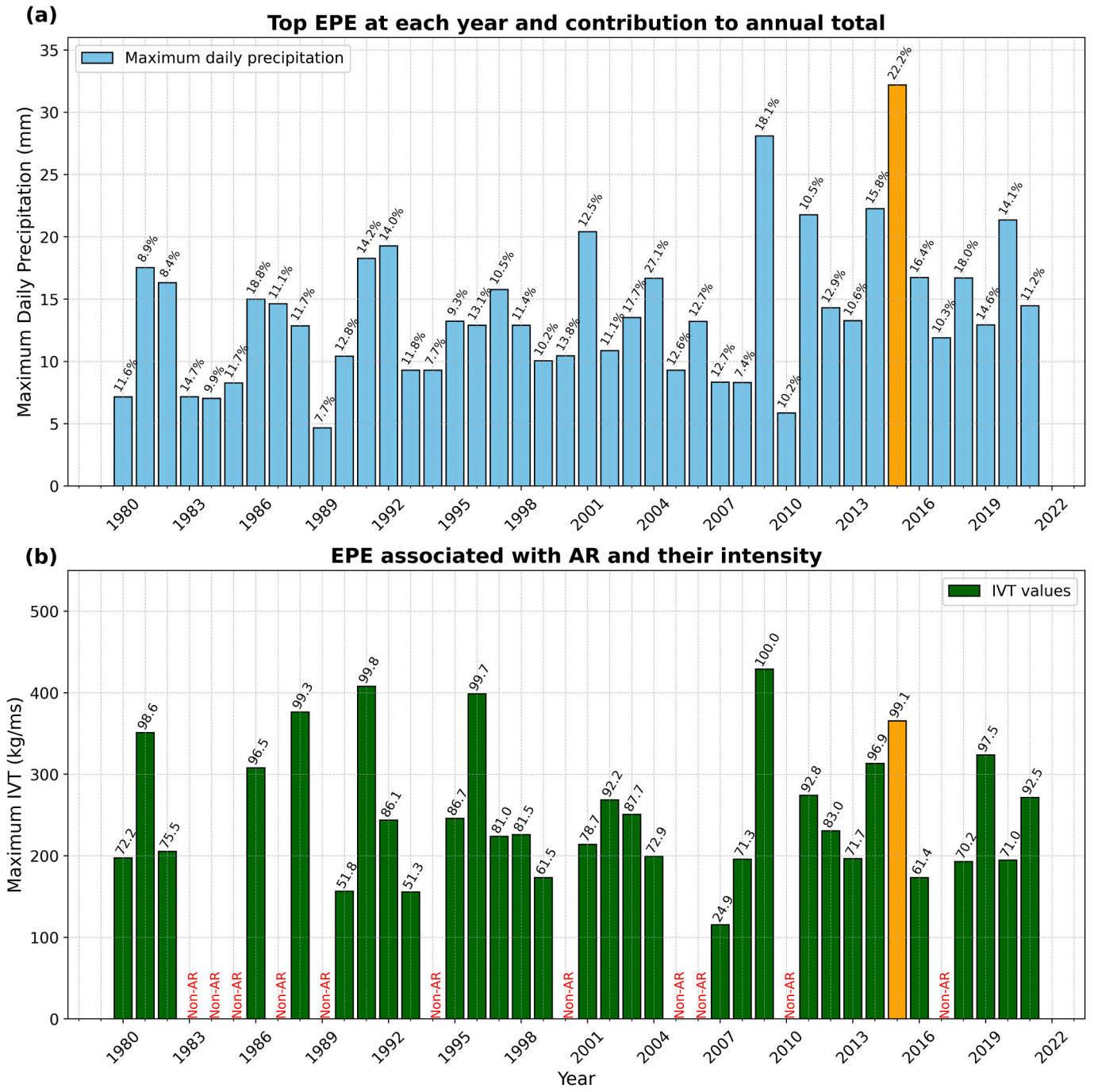

Fig. 12. (a) Histogram showing the precipitation values during the highest precipitation day during each year from 1980 to 2021 at the ice core (IND33) location. The marked percentage values indicate the contribution (three-day accumulated precipitation) from these events to the total annual precipitation. (b) The maximum IVT values during these highest precipitation days and identification of moisture transport patterns as AR and non-AR events using AR detection criteria (Wille et al., 2021). The marked values are the ranking of the AR event, with percentile values as per the distribution of all ARs at the ice core location. A percentile value equal to 100 indicates the strongest AR. The precipitation and IVT values during the event on November 8 and 9, 2015, are marked in different colors.

Prior studies (Baiman et al., 2023; Gorodetskaya et al., 2014; Wille et al., 2021) emphasize the importance of AR-driven precipitation, with an increasing trend in AR occurrences over the past four decades in this region. At coastal locations, ARs make the most significant contribution to snowfall (Maclennan et al., 2022). These ARs can cause surface melt and elevated temperatures (Bozkurt et al., 2018; Gorodetskaya et al., 2023; Wille et al., 2019, 2023) and also influence various aspects of Antarctica, influencing ice sheet and firn properties (Gilbert and Kittel, 2021; Munneke et al., 2014).

Analyzing synoptic patterns of the event using ERA5 data, we reveal quasi-stationary low-pressure systems over the Weddell Sea and an upper-level short-wave trough initiating cyclone formation. Similar patterns of cyclogenesis have been observed in the Indian sector of the Southern Ocean in a study by Turner et al. (2022). Examination of the upper atmosphere indicates a meandering jet stream and the intrusion of a high-pressure ridge eastwards a day before the event. This ridge acted as a block, steering the surface cyclone southwards to landfall over the coast. In other studies, this phenomenon of blocking high-pressure systems in the South Atlantic Ocean has been found to trigger EPEs over East Antarctica (Pohl et al., 2021; Schlosser et al., 2010; Terpstra et al.,

2021). S. Wang et al. (2023) showed that blocking events are made possible by intensified Rossby waves within the circumpolar westerlies, coupled with the advection of warm and moist air through the western flank of these blockings. The research also quantified that these episodes of blocking make a significant contribution, accounting for almost 30 % of EPEs over East Antarctica (S. Wang et al., 2023).

Hourly satellite images illustrated the frontal cyclogenesis, intensified by the warm, moist airmass's advection towards the south. The interaction between the warm airmass from lower latitudes and the cold airmass from Antarctica's interior led to a frontal boundary where a frontal occlusion developed. A jet streak in the upper atmosphere triggered the sudden deepening of the mid-latitude cyclone by enhanced lower-level convergence. It steered the mid-latitude cyclone poleward over the South Atlantic Ocean. Significant moisture uptake occurs in the eastern flank of the cyclone in the South Atlantic Ocean, over the 35°S-40°S band, echoing findings by Terpstra et al. (2021) on the significance of sub-tropical evaporation for high precipitation events in East Antarctica. So, extreme conditions existed in the upper and lower atmosphere during this EPE. This included a strong low-pressure cyclone with a frontal structure, a high-pressure ridge that extended inland, intense moisture moving in as an AR, amplified Rossby waves, and a jet streak in the upper atmosphere.

Complementing the reanalysis data, we employed a high-resolution regional atmospheric model (Polar WRF) to understand the influence of orography on precipitation distribution in coastal DML. Precipitation distribution exhibited a high-low band structure, with more precipitation on the eastern side of steep gradient slopes in the coastal region. Even with intense moisture transport like ARs, local orography heavily influences coastal precipitation. Gehring et al. (2022) also discuss this spatial variation in precipitation distribution, underscoring the importance of local orographic effects in shaping precipitation patterns. Antarctic precipitation hinges on complex mechanisms involving large-scale circulations, precipitation microphysics, local wind patterns, intense moisture transport, and the arrangement of local orography (Gehring et al., 2022; Grazioli et al., 2017). Brief analyses of other EPEs at this location reveal a similar dipole structure of low and high-pressure systems and intense moisture transport similar to ARs from lower latitudes. Thorough case studies can reveal unique atmospheric patterns during such events. At the same time, high-resolution models with improved topographic representation can detail precipitation distribution influenced by local orography and help to explain the small-scale, complex features during precipitation over coastal Antarctica.

As previously discussed, ice core records obtained from coastal locations are significantly influenced by the frequency and intensity of EPEs alongside atmospheric conditions like strong wind velocities and elevated temperatures during these occurrences. These high-temperature synoptic events can introduce bias in stable isotope records, and the post-deposition characteristics are regulated by winds prevailing over complex orographic regions. Consequently, when making choices regarding ice core site selection within these areas, it is imperative to consider both the spatial and temporal distribution of EPEs and their corresponding precipitation distribution patterns.

Per the latest IPCC reports (Intergovernmental Panel On Climate Change, 2023), thermodynamic changes and large-scale circulation patterns could lead to considerable shifts in precipitation extremes with various emission scenarios. With each one degree Celsius of warming in the atmosphere, a 7 % rise in moisture content is projected in the lower atmospheric layers (IPCC chapter 8, (Douville et al., 2021)). This moisture increase is accompanied by intensified wind-driven water transport, particularly towards the convergent zones of atmospheric circulation, including high latitudes. Consequently, an increase in the frequency and intensity of EPEs is anticipated (IPCC Chapter 11, (Seneviratne et al., 2021)). Therefore, a more in-depth analysis of precipitation extremes in Antarctica is essential to enhance our understanding of how these areas will respond to the potential future global climate change.

CRediT authorship contribution statement

Sibin Simon: Writing – original draft, Software, Methodology, Formal analysis, Conceptualization. **John Turner:** Writing – review & editing, Supervision, Methodology, Formal analysis, Conceptualization. **Thamban Meloth:** Writing – review & editing, Supervision, Funding acquisition, Conceptualization. **Pranab Deb:** Writing – review & editing, Supervision, Methodology, Formal analysis. **Irina V. Gorodetskaya:** Writing – review & editing, Data curation. **Matthew Lazzara:** Writing – review & editing, Data curation.

Declaration of competing interest

The authors declare that they have no known competing financial interests or personal relationships that could have appeared to influence the work reported in this paper.

Data availability

ERA5 (Hersbach et al., 2020) data generated by ECMWF are available at the Climate Data Store (https://cds.climate.copernicus.eu/). The hourly snowfall rate from the PE station is published (Souverijns et al. (2017)) and available at https://doi.pangaea.de/10.1594/PANGAEA.913403. SCAR READER database is available online at https://legacy.bas.ac.uk/met/READER/ and observed synoptic data from Neumayer station are also available (König-Langlo (2017)) at https://doi.pangaea.de/10.1594/PANGAEA.858847. The Antarctic satellite composite imagery, infrared and water vapor, are available from the Antarctic Meteorological Research and Data Center Data Repository https://doi.org/10.48567/rm3g-be40. Polar WRF model outputs and further data will be made available on request.

Acknowledgments

We thank the National Centre for Polar and Ocean Research (NCPOR) for facilities and the Ministry of Earth Sciences (Government of India) for financial support through the project "PACER - Cryosphere and Climate." We also appreciate the support of Pratyush HPC facility at IITM, Pune, for modelling works. P. Deb acknowledges the support from the PACER-POP project from NCPOR (grant no. NCPOR/2019/PACER-POP/AS-02). I.V.G. thanks the support by the strategic funding to CIIMAR (UIDB/04423/2020, UIDP/04423/2020), CEEC IND4ed IMPACT (2021.03140.CEECIND/CP1659/CT0005) and project ATLACE (grant no. CIRCNA/CAC/0273/2019) through national funds provided by FCT – Fundação para a Ciência e a Tecnologia, Portugal. M. Lazzara is supported via NSF [grant no - 1924730, 1951603]. The authors also acknowledge HRDG-CSIR for a fellowship grant (grant no. - 09/907 (0009)/2019-EMR-I) to S.Simon. This is NCPOR contribution No. J-31/2024-25.

Appendix A. Supplementary data

Supplementary data to this article can be found online at https://doi.org/10.1016/j.atmosres.2024.107724.

References

Adusumilli, S., A Fish, M., Fricker, H.A., Medley, B., 2021. Atmospheric river precipitation contributed to rapid increases in surface height of the West Antarctic Ice Sheet in 2019. Geophys. Res. Lett. 48 (5), e2020GL091076. https://doi.org/10.1029/2020GL091076.

Baiman, R., Winters, A.C., Lenaerts, J., Shields, C.A., 2023. Synoptic drivers of atmospheric river induced precipitation near dronning Maud Land, Antarctica. J. Geophys. Res. Atmos. 128 (7), e2022JD037859. https://doi.org/10.1029/2022JD037859.

Boening, C., Lebsock, M., Landerer, F., Stephens, G., 2012. Snowfall-driven mass change on the East Antarctic ice sheet. Geophys. Res. Lett. 39 (21). https://doi.org/10.1029/2012GL053316.

Bozkurt, D., Rondanelli, R., Marín, J.C., Garreaud, R., 2018. Foehn event triggered by an atmospheric river underlies record-setting temperature along Continental Antarctica. J. Geophys. Res. Atmos. 123 (8), 3871–3892. https://doi.org/10.1002/2017JD027796.

Bromwich, D.H., 1988. Snowfall in high southern latitudes. Rev. Geophys. 26 (1), 149–168. https://doi.org/10.1029/RG026i001p00149.

Bromwich, D.H., Otieno, F.O., Hines, K.M., Manning, K.W., Shilo, E., 2013. Comprehensive evaluation of polar weather research and forecasting model performance in the Antarctic. J. Geophys. Res. Atmos. 118 (2), 274–292. https://doi.org/10.1029/2012JD018139.

Dalaiden, Q., Goosse, H., Lenaerts, J.T.M., Cavitte, M.G.P., Henderson, N., 2020. Future Antarctic snow accumulation trend is dominated by atmospheric synoptic-scale events. Commun. Earth Environ. 1 (1), 62. https://doi.org/10.1038/s43247-020-00062-x.

Danielson, J.J., Gesch, D.B., 2011. Global Multi-resolution Terrain Elevation Data 2010 (GMTED2010) (n.d.).

Dattler, M.E., Lenaerts, J.T.M., Medley, B., 2019. Significant spatial variability in radar-derived West Antarctic accumulation linked to surface winds and topography. Geophys. Res. Lett. 46 (22), 13126–13134. https://doi.org/10.1029/2019GL085363.

Davison, B.J., Hogg, A.E., Rigby, R., Veldhuijsen, S., van Wessem, J.M., van den Broeke, M.R., Holland, P.R., Selley, H.L., Dutrieux, P., 2023. Sea level rise from West Antarctic mass loss significantly modified by large snowfall anomalies. Nat. Commun. 14 (1). https://doi.org/10.1038/s41467-023-36990-3. Article 1.

Deb, P., Orr, A., Hosking, J.S., Phillips, T., Turner, J., Bannister, D., Pope, J.O., Colwell, S., 2016. An assessment of the Polar Weather Research and Forecasting (WRF) model representation of near-surface meteorological variables over West Antarctica. J. Geophys. Res. Atmos. 121 (4), 1532–1548. https://doi.org/10.1002/2015JD024037.

Dennison, F.W., McDonald, A., Morgenstern, O., 2016. The influence of ozone forcing on blocking in the Southern Hemisphere. J. Geophys. Res. Atmos. 121 (24), 14,358–14,371. https://doi.org/10.1002/2016JD025033.

Douville, H., Raghavan, K., Renwick, J.A., Allan, R.P., Arias, P.A., Barlow, M., Cerezo Mota, R., Cherchi, A., Gan, T.Y., Gergis, J., Jiang, D., Khan, A., Pokam Mba, W., Rosenfeld, D., Tierney, J., Zolina, O., 2021. Water cycle changes. In: Masson-Delmotte, V., Zhai, P., Pirani, A., Connors, S.L., Péan, C., Berger, S., Caud, N., Chen, Y., Goldfarb, L., Gomis, M.I., Huang, M., Leitzell, K., Lonnoy, E., Matthews, J. B.R., Maycock, T.K., Waterfield, T., Yelekçi, Ö., Yu, R., Zhou, B. (Eds.), Climate Change 2021: The Physical Science Basis. Contribution of Working Group I to the Sixth Assessment Report of the Intergovernmental Panel on Climate Change. Cambridge University Press, pp. 1055–1210. https://doi.org/10.1017/9781009157896.001.

Ejaz, T., Rahaman, W., C M, L., Mahalinganathan, K., Thamban, M., 2021. Sea ice variability and trends in the Western Indian Ocean sector of Antarctica during the past two centuries and its response to climatic modes. J. Geophys. Res. Atmos. 126. https://doi.org/10.1029/2020JD033943.

Francis, D., Mattingly, K.S., Lhermitte, S., Temimi, M., Heil, P., 2021. Atmospheric extremes caused high oceanward sea surface slope triggering the biggest calving event in more than 50 years at the Amery Ice Shelf. Cryosphere 15 (5), 2147–2165. https://doi.org/10.5194/tc-15-2147-2021.

Gehring, J., Vignon, É., Billault-Roux, A.-C., Ferrone, A., Protat, A., Alexander, S.P., Berne, A., 2022. Orographic flow influence on precipitation during an atmospheric river event at Davis, Antarctica. J. Geophys. Res. Atmos. 127 (2), e2021JD035210. https://doi.org/10.1029/2021JD035210.

Gilbert, E., Kittel, C., 2021. Surface melt and runoff on Antarctic Ice shelves at 1.5°C, 2°C, and 4°C of future warming. Geophys. Res. Lett. 48 (8), e2020GL091733. https://doi.org/10.1029/2020GL091733.

Gorodetskaya, I.V., Silva, T., Schmithüsen, H., et al., 2020. Atmospheric River Signatures in Radiosonde Profiles and Reanalyses at the Dronning Maud Land Coast, East Antarctica. Adv. Atmos. Sci. 37, 455–476. https://doi.org/10.1007/s00376-020-9221-8.

Gorodetskaya, I.V., Tsukernik, M., Claes, K., Ralph, M.F., Neff, W.D., Lipzig, N.P.M.V., 2014. The role of atmospheric rivers in anomalous snow accumulation in East Antarctica. Geophys. Res. Lett. 41 (17), 6199–6206. https://doi.org/10.1002/2014GL060881.

Gorodetskaya, I.V., Kneifel, S., Maahn, M., Van Tricht, K., Thiery, W., Schween, J.H., Mangold, A., Crewell, S., Van Lipzig, N.P.M., 2015. Cloud and precipitation properties from ground-based remote-sensing instruments in East Antarctica. Cryosphere 9 (1), 285–304. https://doi.org/10.5194/tc-9-285-2015.

Gorodetskaya, I.V., Durán-Alarcón, C., González-Herrero, S., Clem, K.R., Zou, X., Rowe, P., Rodriguez Imazio, P., Campos, D., Leroy-Dos Santos, C., Dutrievoz, N., Wille, J.D., Chyhareva, A., Favier, V., Blanchet, J., Pohl, B., Cordero, R.R., Park, S.-J., Colwell, S., Lazzara, M.A., Picard, G., 2023. Record-high Antarctic Peninsula temperatures and surface melt in February 2022: a compound event with an intense atmospheric river. Npj Clim. Atmos. Sci. 6 (1). https://doi.org/10.1038/s41612-023-00529-6. Article 1.

Grazioli, J., Genthon, C., Boudevillain, B., Duran-Alarcon, C., Del Guasta, M., Madeleine, J.-B., Berne, A., 2017. Measurements of precipitation in Dumont d'Urville, Adélie Land, East Antarctica. Cryosphere 11 (4), 1797–1811. https://doi.org/10.5194/tc-11-1797-2017.

Grieger, J., Leckebusch, G.C., Raible, C.C., Rudeva, I., Simmonds, I., 2018. Subantarctic cyclones identified by 14 tracking methods, and their role for moisture transports into the continent. Tellus A 70 (1), 1–18. https://doi.org/10.1080/16000870.2018.1454808.

Grise, K.M., Medeiros, B., Benedict, J.J., Olson, J.G., 2019. Investigating the influence of cloud radiative effects on the extratropical storm tracks. Geophys. Res. Lett. 46 (13), 7700–7707. https://doi.org/10.1029/2019GL083542.

Hersbach, H., Bell, B., Berrisford, P., Hirahara, S., Horányi, A., Muñoz-Sabater, J., Nicolas, J., Peubey, C., Radu, R., Schepers, D., Simmons, A., Soci, C., Abdalla, S., Abellan, X., Balsamo, G., Bechtold, P., Biavati, G., Bidlot, J., Bonavita, M., Thépaut, J.-N., 2020. The ERA5 global reanalysis. Q. J. R. Meteorol. Soc. 146 (730), 1999–2049. https://doi.org/10.1002/qj.3803.

Hines, K.M., Bromwich, D.H., 2008. Development and testing of Polar Weather Research and Forecasting (WRF) model. Part I: Greenland Ice sheet meteorology. Mon. Weather Rev. 136 (6), 1971–1989. https://doi.org/10.1175/2007MWR2112.1.

Intergovernmental Panel On Climate Change, 2023. Climate Change 2021 – The Physical Science Basis. In: Working Group I Contribution to the Sixth Assessment Report of the Intergovernmental Panel on Climate Change, 1st ed. Cambridge University Press. https://doi.org/10.1017/9781009157896.

Kohrs, R.A., Lazzara, M.A., Robaidek, J.O., Santek, D.A., Knuth, S.L., 2014. Global satellite composites—20 years of evolution. Atmos. Res. 135–136, 8–34. https://doi.org/10.1016/j.atmosres.2013.07.023.

Lazzara, M.A., Keller, L.M., Stearns, C.R., Thom, J.E., Weidner, G.A., 2003. Antarctic satellite meteorology: applications for weather forecasting. Mon. Weather Rev. 131 (2), 371–383. https://doi.org/10.1175/1520-0493(2003)131<0371:ASMAFW>2.0.CO;2.

Lenaerts, J.T.M., van den Broeke, M.R., Déry, S.J., van Meijgaard, E., van de Berg, W.J., Palm, S.P., Sanz Rodrigo, J., 2012. Modeling drifting snow in Antarctica with a regional climate model: 1. Methods and model evaluation. J. Geophys. Res.-Atmos. 117 (D5). https://doi.org/10.1029/2011JD016145.

Lenaerts, J.T.M., van Meijgaard, E., van den Broeke, M.R., Ligtenberg, S.R.M., Horwath, M., Isaksson, E., 2013. Recent snowfall anomalies in Dronning Maud Land, East Antarctica, in a historical and future climate perspective. Geophys. Res. Lett. 40 (11), 2684–2688. https://doi.org/10.1002/grl.50559.

Maclennan, M.L., Lenaerts, J.T.M., 2021. Large-scale atmospheric drivers of snowfall over Thwaites Glacier, Antarctica. Geophys. Res. Lett. 48 (17), e2021GL093644. https://doi.org/10.1029/2021GL093644.

Maclennan, M.L., Lenaerts, J.T.M., Shields, C., Wille, J.D., 2022. Contribution of atmospheric rivers to Antarctic precipitation. Geophys. Res. Lett. 49 (18), e2022GL100585. https://doi.org/10.1029/2022GL100585.

Medley, B., Thomas, E.R., 2019. Increased snowfall over the Antarctic Ice Sheet mitigated twentieth-century sea-level rise. Nat. Clim. Chang. 9 (1). https://doi.org/10.1038/s41558-018-0356-x. Article 1.

Mottram, R., Hansen, N., Kittel, C., van Wessem, J.M., Agosta, C., Amory, C., Boberg, F., van de Berg, W.J., Fettweis, X., Gossart, A., van Lipzig, N.P.M., van Meijgaard, E., Orr, A., Phillips, T., Webster, S., Simonsen, S.B., Souverijns, N., 2021. What is the surface mass balance of Antarctica? An intercomparison of regional climate model estimates. Cryosphere 15 (8), 3751–3784. https://doi.org/10.5194/tc-15-3751-2021.

Munneke, P.K., Ligtenberg, M., R, S., van den Broeke, M.R., van Angelen, J.H., Forster, R. R., 2014. Explaining the presence of perennial liquid water bodies in the firn of the Greenland Ice Sheet. Geophys. Res. Lett. 41 (2), 476–483. https://doi.org/10.1002/2013GL058389.

Noone, D., Turner, J., Mulvaney, R., 1999. Atmospheric signals and characteristics of accumulation in Dronning Maud Land, Antarctica. J. Geophys. Res.-Atmos. 104 (D16), 19191–19211. https://doi.org/10.1029/1999JD900376.

Pohl, B., Favier, V., Wille, J., Udy, D.G., Vance, T.R., Pergaud, J., Dutrievoz, N., Blanchet, J., Kittel, C., Amory, C., Krinner, G., Codron, F., 2021. Relationship between weather regimes and atmospheric rivers in East Antarctica. J. Geophys. Res. Atmos. 126 (24), e2021JD035294. https://doi.org/10.1029/2021JD035294.

Reboita, M.S., da Rocha, R.P., Ambrizzi, T., Gouveia, C.D., 2015. Trend and teleconnection patterns in the climatology of extratropical cyclones over the Southern Hemisphere. Clim. Dyn. 45 (7), 1929–1944. https://doi.org/10.1007/s00382-014-2447-3.

Rotschky, G., Holmlund, P., Isaksson, E., Mulvaney, R., Oerter, H., Broeke, M.R.V.D., Winther, J.-G., 2007. A new surface accumulation map for western Dronning Maud Land, Antarctica, from interpolation of point measurements. J. Glaciol. 53 (182), 385–398. https://doi.org/10.3189/002214307783258459.

Schlosser, E., Powers, J.G., Duda, M.G., Manning, K.W., Reijmer, C.H., van den Broeke, M.R., 2010. An extreme precipitation event in Dronning Maud Land, Antarctica: a case study with the Antarctic Mesoscale Prediction System. Polar Res. 29 (3), 330–344. https://doi.org/10.3402/polar.v29i3.6072.

Schlosser, E., Dittmann, A., Stenni, B., Powers, J.G., Manning, K.W., Masson-Delmotte, V., Valt, M., Cagnati, A., Grigioni, P., Scarchilli, C., 2017. The influence of the synoptic regime on stable water isotopes in precipitation at Dome C, East Antarctica. Cryosphere 11 (5), 2345–2361. https://doi.org/10.5194/tc-11-2345-2017.

Seneviratne, S.I., Zhang, X., Adnan, M., Badi, W., Dereczynski, C., Di Luca, A., Ghosh, S., Iskandar, I., Kossin, J., Lewis, S., Otto, F., Pinto, I., Satoh, M., Vicente-Serrano, S.M., Wehner, M., Zhou, B., 2021. Weather and climate extreme events in a changing climate. In: Masson-Delmotte, V., Zhai, P., Pirani, A., Connors, S.L., Péan, C., Berger, S., Caud, N., Chen, Y., Goldfarb, L., Gomis, M.I., Huang, M., Leitzell, K., Lonnoy, E., Matthews, J.B.R., Maycock, T.K., Waterfield, T., Yelekçi, Ö., Yu, R., Zhou, B. (Eds.), Climate Change 2021: The Physical Science Basis. Contribution of Working Group I to the Sixth Assessment Report of the Intergovernmental Panel on Climate Change. Cambridge University Press, pp. 1513–1766. https://doi.org/10.1017/9781009157896.001.

Servettaz, A.P.M., Orsi, A.J., Curran, M.A.J., Moy, A.D., Landais, A., Agosta, C., Winton, V.H.L., Touzeau, A., McConnell, J.R., Werner, M., Baroni, M., 2020. Snowfall and water stable isotope variability in East Antarctica controlled by warm

synoptic events. J. Geophys. Res. Atmos. 125 (17), e2020JD032863. https://doi.org/10.1029/2020JD032863.

Simon, S., Turner, J., Thamban, M., Wille, J.D., Deb, P., 2024. Spatiotemporal variability of extreme precipitation events and associated atmospheric processes over dronning Maud Land, East Antarctica. J. Geophys. Res. Atmos. 129 (7), e2023JD038993. https://doi.org/10.1029/2023JD038993.

Solman, S.A., Orlanski, I., 2014. Poleward shift and change of frontal activity in the Southern Hemisphere over the last 40 years. J. Atmos. Sci. 71 (2), 539–552. https://doi.org/10.1175/JAS-D-13-0105.1.

Souverijns, N., Gossart, A., Gorodetskaya, I.V., Lhermitte, S., Mangold, A., Laffineur, Q., Delcloo, A., van Lipzig, N.P.M., 2018. How does the ice sheet surface mass balance relate to snowfall? Insights from a ground-based precipitation radar in East Antarctica. Cryosphere 12 (6), 1987–2003. https://doi.org/10.5194/tc-12-1987-2018.

Souverijns, N., Gossart, A., Lhermitte, S., Gorodetskaya, I.V., Kneifel, S., Maahn, M., Bliven, F.L., van Lipzig, N.P.M., 2017. Estimating radar reflectivity—Snowfall rate relationships and their uncertainties over Antarctica by combining disdrometer and radar observations. Atmospheric Research 196, 211–223. https://doi.org/10.1016/j.atmosres.2017.06.001.

Swetha Chittella, S.P., Deb, P., Melchior van Wessem, J., 2022. Relative contribution of atmospheric drivers to “extreme” snowfall over the Amundsen Sea embayment. Geophys. Res. Lett. 49 (16), e2022GL098661. https://doi.org/10.1029/2022GL098661.

Terpstra, A., Gorodetskaya, I.V., Sodemann, H., 2021. Linking sub-tropical evaporation and extreme precipitation over East Antarctica: an atmospheric river case study. J. Geophys. Res. Atmos. 126 (9), e2020JD033617. https://doi.org/10.1029/2020JD033617.

Turner, J., Colwell, S.R., Marshall, G.J., Lachlan-Cope, T.A., Carleton, A.M., Jones, P.D., Lagun, V., Reid, P.A., Iagovkina, S., 2004. The SCAR READER project: toward a high-quality database of mean Antarctic meteorological observations. J. Clim. 17 (14), 2890–2898. https://doi.org/10.1175/1520-0442(2004)017<2890:TSRPTA>2.0.CO;2.

Turner, J., Phillips, T., Thamban, M., Rahaman, W., Marshall, G.J., Wille, J.D., Favier, V., Winton, V.H.L., Thomas, E., Wang, Z., van den Broeke, M., Hosking, J.S., Lachlan-Cope, T., 2019. The dominant role of extreme precipitation events in Antarctic snowfall variability. Geophys. Res. Lett. 46 (6), 3502–3511. https://doi.org/10.1029/2018GL081517.

Turner, J., Lu, H., King, J.C., Carpentier, S., Lazzara, M., Phillips, T., Wille, J., 2022. An extreme high temperature event in Coastal East Antarctica associated with an atmospheric river and record summer downslope winds. Geophys. Res. Lett. 49 (4), e2021GL097108. https://doi.org/10.1029/2021GL097108.

Wang, X.L., Feng, Y., Chan, R., Isaac, V., 2016. Inter-comparison of extra-tropical cyclone activity in nine reanalysis datasets. Atmos. Res. 181, 133–153. https://doi.org/10.1016/j.atmosres.2016.06.010.

Wang, S., Ding, M., Liu, G., Li, G., Chen, W., 2023. Blocking events in East Antarctica: impact on precipitation and their association with large-scale atmospheric circulation modes. J. Clim. 1 (aop). https://doi.org/10.1175/JCLI-D-23-0419.1.

Welker, C., Martius, O., Froidevaux, P., Reijmer, C.H., Fischer, H., 2014. A climatological analysis of high-precipitation events in Dronning Maud Land, Antarctica, and associated large-scale atmospheric conditions. J. Geophys. Res. Atmos. 119 (21), 11,932–11,954. https://doi.org/10.1002/2014JD022259.

Wille, J.D., Favier, V., Dufour, A., Gorodetskaya, I.V., Turner, J., Agosta, C., Codron, F., 2019. West Antarctic surface melt triggered by atmospheric rivers. Nat. Geosci. 12 (11). https://doi.org/10.1038/s41561-019-0460-1. Article 11.

Wille, J.D., Favier, V., Gorodetskaya, I.V., Agosta, C., Kittel, C., Beeman, J.C., Jourdain, N.C., Lenaerts, J.T.M., Codron, F., 2021. Antarctic atmospheric river climatology and precipitation imPACTS. J. Geophys. Res. Atmos. 126 (8), e2020JD033788. https://doi.org/10.1029/2020JD033788.

Wille, J.D., Favier, V., Jourdain, N.C., Kittel, C., Turton, J.V., Agosta, C., Gorodetskaya, I.V., Picard, G., Codron, F., Santos, C.L.-D., Amory, C., Fettweis, X., Blanchet, J., Jomelli, V., Berchet, A., 2022. Intense atmospheric rivers can weaken ice shelf stability at the Antarctic Peninsula. Commun. Earth Environ. 3 (1). https://doi.org/10.1038/s43247-022-00422-9. Article 1.

Wille, J.D., Alexander, S.P., Amory, C., Baiman, R., Barthélemy, L., Bergstrom, D.M., Berne, A., Binder, H., Blanchet, J., Bozkurt, D., Bracegirdle, T.J., Casado, M., Choi, T., Clem, K.R., Codron, F., Datta, R., Battista, S.D., Favier, V., Francis, D., Zou, X., 2023. The extraordinary March 2022 East Antarctica “heat” wave. Part II: impacts on the Antarctic ice sheet. J. Clim. 1 (aop). https://doi.org/10.1175/JCLI-D-23-0176.1.

Yu, L., Yang, Q., Vihma, T., Jagovkina, S., Liu, J., Sun, Q., Li, Y., 2018. Features of extreme precipitation at progress station, Antarctica. J. Clim. 31 (22), 9087–9105. https://doi.org/10.1175/JCLI-D-18-0128.1.

Zou, X., Rowe, P.M., Gorodetskaya, I., Bromwich, D.H., Lazzara, M., Cordero, R.R., Zhang, Z., Kawzenuk, B., Cordeira, J.M., Wille, J.D., Ralph, F.M., Bai, L., 2022. Strong warming over the Antarctic Peninsula during combined atmospheric river and Foehn events: contribution of shortwave radiation and turbulence [Preprint]. Atmos. Sci. https://doi.org/10.1002/essoar.10512808.1.